processes

MDPI

*Article*

# Curvature-Adaptive Compact Triple-Band Metamaterial Uniplanar Compact Electromagnetic Bandgap-Based Printed Antenna for Wearable Wireless and Medical Body Area Network Applications

**Tarek Messatfa [1,*], Souad Berhab [2], Fouad Chebbara [1] and Mohamed S. Soliman [3,*]**

[1] Electrical Engineering Laboratory (LAGE), Department of Electronics and Telecommunications, Faculty of Sciences and Technology, University of Kasdi Merbah, Ouargla 30000, Algeria; chebbara.fouad@univ-ouargla.dz
[2] LARATIC Laboratory, Higher National School of Telecommunications and Information and Communication Technologies-ENSTTIC, Oran 31000, Algeria; souad.berhab@ensttic.dz
[3] Department of Electrical Engineering, College of Engineering, Taif University, Taif 21944, Saudi Arabia
* Correspondence: messatfa.tarek@univ-ouargla.dz (T.M.); soliman@tu.edu.sa (M.S.S.)

**Abstract:** A novel, compact, monopole apple-shaped, triple-band metamaterial-printed wearable antenna backed by a uniplanar compact electromagnetic bandgap (UC-EBG) structure is introduced in this paper for wearable wireless and medical body area network (WBAN/MBAN) applications. A tri-band UC-EBG structure has been utilized as a ground plane to minimize the impact of antenna radiation on the human body and improve antenna performance for the proposed wearable antenna. Metamaterial triangular complementary split ring resonators (TCSRRs) are incorporated into the antenna and UC-EBG structure, resulting in a compact UC-EBG-backed antenna with an overall size of $39 \times 39 \times 2.84$ mm$^3$ ($0.41\ \lambda_g \times 0.41\ \lambda_g \times 0.029\ \lambda_g$). The printed textile antenna operates at 2.45 GHz for the wireless local area network (WLAN), 3.5 GHz for 5G new radio (NR), and 5.8 GHz for the industrial, scientific, and medical (ISM) bands with improved gain and high-efficiency values. Furthermore, the performance of the antenna is analyzed on the human body, where three models of curved body parts are considered: a child's arm (worst case) with a 40 mm radius, an adult's arm with a 60 mm radius, and an adult's leg with a 70 mm radius. The results demonstrate that the proposed antenna is an attractive candidate for wearable healthcare and fitness monitoring devices and other WBAN/MBAN applications due to its compact size, high performance, and low SAR values.

**Keywords:** 5G NR; apple-shaped wearable antenna; ISM; metamaterial; SAR; TCSRRs; triple-band; UC-EBG; WBAN/MBAN; WLAN



**Citation:** Messatfa, T.; Berhab, S.; Chebbara, F.; Soliman, M.S. Curvature-Adaptive Compact Triple-Band Metamaterial Uniplanar Compact Electromagnetic Bandgap-Based Printed Antenna for Wearable Wireless and Medical Body Area Network Applications. *Processes* **2024**, *12*, 1380. https://doi.org/10.3390/pr12071380

Academic Editor: Enrique Rosales-Asensio

Received: 1 June 2024
Revised: 23 June 2024
Accepted: 29 June 2024
Published: 2 July 2024



## 1. Introduction

Recent progress in wireless communications has revolutionized and significantly transformed our everyday utilization and engagement with technology. Wireless technology such as cell phones, computers, smartwatches, fitness monitors, and wearable devices has made long-distance communication and information exchange more readily available.

Wearable printed antennas have recently attracted considerable interest due to their versatility, lightweight, compactness, and importance in facilitating wireless communication between wearable and Internet of Things (IoT) devices, which make them suitable for multiple applications in Wireless Body Area Networks (WBAN) [1]. Furthermore, these antennas are designed to be compact and flexible to ensure compatibility with devices like smartwatches and fitness trackers. When these antennas are incorporated into mobile and wearable devices on the body, they facilitate seamless communication and data transfer between the wearable and other networked devices, allowing the adoption of wearable devices in different domains, including health monitoring and fitness tracking [2,3].

However, since wearable printed antennas are usually worn near the body, they have a high Specific Absorption Rate (SAR) level due to antenna back radiation. Therefore, wearable printed antennas backed by EBG (electromagnetic bandgap) structures have been of interest to researchers as a solution to the issue of high SAR levels in wearable patch antennas. In this work, UC-EBG (uniplanar compact electromagnetic bandgap) structures are used instead of the conventional EBG structures due to their uniplanar feature, which eliminates the requirement for via-holes or a multilayer substrate, thus simplifying implementation and reducing fabrication costs compared to conventional EBGs [4].

Integrating UC-EBG structures into the design of printed antennas provides many advantages, such as the suppression of surface wave propagation, the improvement of radiation efficiency, and the reduction in interference. They also reduce the SAR level, improving safety and protecting the body from back-antenna radiation. This feature makes UC-EBG-based wearable printed antennas an appropriate choice for WBAN applications, protecting human health and limiting the potential dangers of electromagnetic exposure [5,6].

A compact printed antenna working in the (2.4–2.5 GHz) ISM band was introduced in [7] for medical applications. It is printed on a Rogers Duroid RT-5880 substrate with a total dimension of $60 \times 60$ mm$^2$ ($0.73\ \lambda_g \times 0.73\ \lambda_g$) and a bandwidth of 2.45–2.5 GHz (4.1%). A novel wearable multiband antenna using a complete ground plane was designed in [8] for WBAN applications. It operates at 2.45/5 GHz WLAN bands in addition to the UWB high band. It offers a directional radiation pattern and has a total size of $84 \times 69 \times 3.4$ mm$^3$ ($0.69\ \lambda_g \times 0.57\ \lambda_g \times 0.028\ \lambda_g$) using 3.2 mm thick PF4 foam as a substrate. The authors used multi-resonant radiators and slots to achieve a multiband antenna, covering 2.4–2.5 GHz (4%) and 4.6–6 GHz (32%) bandwidths, including the UWB standard.

In [9], the authors proposed a printed dual-band antenna incorporating an SRR and EBG for use in wearable sensor networks for IoT applications. The antenna operates at 2.4 GHz and 5.4 GHz and has dimensions of $157 \times 157 \times 3$ mm$^3$ ($1.54\ \lambda_g \times 1.54\ \lambda_g \times 0.029\ \lambda_g$). Both conventional and metamaterial-based antennas were fabricated using a washable cotton substrate. It achieved an operating bandwidth of 3.29% at the lower band and 6.92% at the upper band. The antenna based on SRR exhibited a higher gain and effectively reduced the surface waves. Nevertheless, the antenna suffers from its large size and limited width, as well as the manufacturing difficulty resulting from the use of EBG structures as compared to UC-EBG, which is uniplanar and does not require via-holes in the substrate.

A compact AMC-structured dual-band textile antenna for WBAN/WLAN applications was presented in [10]. The antenna size is $66 \times 40 \times 4$ mm$^3$ ($0.59\ \lambda_g \times 0.36\ \lambda_g \times 0.03\ \lambda_g$), which is placed on a felt substrate and operates at both 2.45 GHz and 5.8 GHz frequencies with a fractional bandwidth of 65.3% and 62.06% at 2.45/5.8 GHz, respectively. Utilizing a dual hexagonal AMC structure resulted in acceptable SAR values. While the proposed antenna exhibits a wide bandwidth, its dimension is comparatively large.

According to [11], an EBG-loaded coplanar wearable antenna operating in three frequency bands has been presented for wearable devices. The antenna provides coverage for both WLAN and sub-6-GHz 5G applications. A felt substrate measuring $69 \times 69 \times 5$ mm$^3$ ($0.61\ \lambda_g \times 0.61\ \lambda_g \times 0.04\ \lambda_g$) was used to fabricate both the EBG and the monopole textile antenna. It has a bandwidth of 10%, 16%, and 7%, with a gain of 5.11, 6.43, and 7.4 dBi at 2.4/3.5/5.8 GHz, respectively. The presence of the EBG caused a significant reduction of over 91% in the calculated SAR values for the antenna. The presented antenna is an attractive choice for wearable applications due to its tri-band operation, good radiation performance, and low SAR. However, its considerable size makes it challenging to include in compact wearable devices.

Another low-profile tri-band antenna based on an artificial magnetic conductor (AMC) was designed for WBAN applications [12]. The antenna is a flexible tri-ring monopole with AMC worn on the body. A tri-band AMC structure is incorporated to reduce the SAR level. It was designed to operate at three frequency bands (2.4/3.5/5.8 GHz), with respective

bandwidths of 2.28–2.51 GHz (9.6%), 3.5–4.5 GHz (25%), and 5.5–5.8 GHz (8.7%). The antenna and AMC were printed on a 3.5 dielectric constant flexible polyimide film. The antenna exhibits peak gains of 4.8, 5.1, and 6.2 dBi at 2.4/3.5/5.8 GHz, respectively. However, the overall dimensions of the antenna are $90 \times 90 \times 6$ mm$^3$ ($1.34\ \lambda_g \times 1.34\ \lambda_g \times 0.09\ \lambda_g$), which is relatively large for wearable devices.

This paper introduces an innovative, compact, and tri-band apple-shaped textile antenna inspired by metamaterials and backed by an UC-EBG structure for WBAN applications. The designed antenna is created to operate within the WLAN and ISM bands (2.45/5.8 GHz), making it appropriate for WBAN applications such as fitness tracking and healthcare monitoring. Additionally, it operates in the 5G-NR (3.5 GHz) band, which is used for 5G networks, applications related to smart cities, and vehicle-to-everything (V2X) communications. The antenna employs double TCSRR-metamaterial structures to make it as lightweight and compact as possible, ensuring comfort during wear. Further, to achieve a good deformation recovery ability, the antenna uses jeans as its substrate, which is very flexible and has very low losses ($\tan\delta$ = 0.0033). The robustness of the UC-EBG-based textile antenna is examined by studying its bending characteristics on the human body, which significantly reduces SAR values and enhances antenna efficiency.

## 2. Proposed MTM Unit Cell Design and Novel Antenna Configuration

### *2.1. TCSRR-MTM Unit Cell*

The metamaterial triangular complementary split-ring resonator (TCSRR) is a modified version of the CSRR structure widely utilized in the design of printed antennas to achieve the desired performance without altering the antenna size [13–16]. According to [17], the TCSRR outperforms metamaterial shapes such as rectangular, circular, pentagonal, and hexagonal in terms of frequency band coverage, return loss, bandwidth, and total area. When the TCSRR metamaterial structure is incorporated into the printed antenna, it alters the distribution of the current on the radiating patch, leading to the generation of new or multiple resonant frequencies while maintaining the same total size of the antenna. Adjusting the size and geometry of the TCSRR allows specific frequencies to be generated, providing flexibility in designing patch antennas for various applications. In [18], TSRR achieves three negative frequency bands with a single unit structure containing multiple rings, but its implementation requires more area.

Two TCSRRs-MTM structures are presented in this study. The first structure is the L-TCSRR, a modified version of the TCSRR. It has an L-slot added to the ends of its edges (Figure 1a) to resonate at 2.45 GHz without occupying more space on the patch antenna. The second TCSRR structure (Figure 1b) resonates at 5.8 GHz.

The proposed TCSRRs-MTM (Figure 1c) is designed on a jeans textile substrate with a dielectric constant ($\varepsilon_r$ = 1.67) and a thickness of 2.84 mm. This design aims to achieve a compact tri-band printed antenna. Figure 1a–e illustrates the geometrical view of the TCSRR and L-TCSRR unit cells, their corresponding equivalent circuit model (ECM), and the final TCSRR structure design with its ECM.

The TCSRR acts as a resonant LC circuit, where the inner and outer metal sheets generate the inductance and the ring slot in the metal sheets creates the capacitance. The resonance frequency $f_0$ for each unit cell of the TCSRR structure is determined by the following equations [19]:

$$f_0 = \frac{1}{2\pi\sqrt{LC}} \tag{1}$$

$$L = \frac{3\mu_0\mu_r}{2\pi}\left(ln\left(\frac{T}{w}\right) - 1.405\right) \tag{2}$$

$$C = 0.75TC_{pul} \tag{3}$$

$$C_{pul} = \frac{\sqrt{\varepsilon_{eff}}}{cZ_0} \quad (4)$$

where the equivalent TCSRR inductance and capacitance are represented by $L$ and $C$, respectively. $C_{pul}$ refers to the effective length capacitance, $\mu_r$ and $\mu_{0,}$ are the dielectric material and free space relative permeability, respectively, while $\varepsilon_{eff}$ is the effective permittivity of the dielectric material. $w$ and $T$ represent the TCSRR structure's gap width and side length, respectively. $Z_0$ represents the free space characteristic impedance, while $c$ denotes the speed of light ($3 \times 10^8$ m/s).

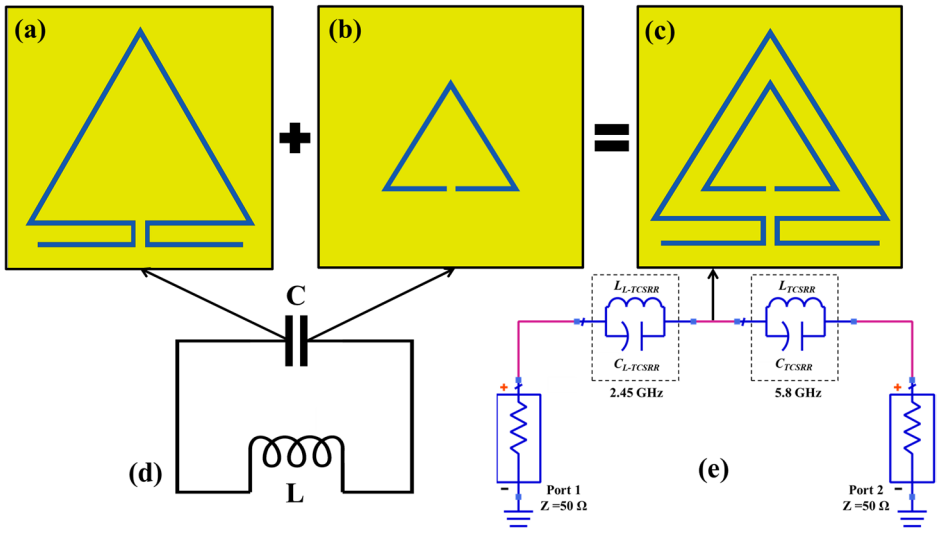


**Figure 1.** (**a**) L-TCSRR structure (2.45 GHz), (**b**) TCSRR structure (5.8 GHz), (**c**) final TCSRRs-MTM unit cell design, (**d**) ECM of TCSRR, and (**e**) ECM of the final proposed TCSRR-MTM structure.

The simulated TCSRR surface current distribution at 2.45/5.8 GHz is shown in Figure 2a,b. It is apparent that at 2.45 GHz, the current loops around L-TCSRR (Figure 2a), while at 5.8 GHz, it circulates around the inner TCSRR (Figure 2b). According to the analysis of the current distribution, it has been determined that L-TCSRR is responsible for 2.45 GHz, whereas the inner TCSRR is responsible for 5.8 GHz.

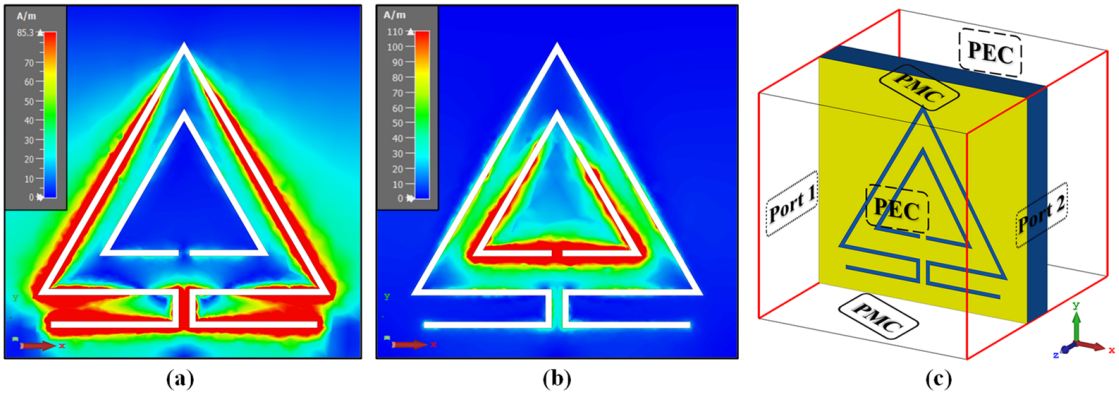


**Figure 2.** TCSRR-MTM current distributions: (**a**) 2.45 GHz, (**b**) 5.8 GHz, and (**c**) the boundary conditions configuration of the TCSRR-MTM unit cell for retrieving the S-parameter.

To demonstrate that the TCSRR structure exhibits a negative-permittivity (ENG) metamaterial behavior at the required frequencies, the TCSRR unit cell is analyzed, and its scattering parameters are calculated to extract its effective permittivity ($\varepsilon$). This is achieved by applying boundary conditions of the TEM environment to the waveguide faces and stimulating them with the TEM wave, as represented in Figure 2c. On the upper and lower

sides of the waveguide, the perfect magnetic conductors (PMCs) are designated, while on the right and left sides, the waveguide port (Port 1 and Port 2) is defined. The remaining faces along the *z*-axis are designated as perfect electric conductors (PECs).

TCSRR-MTM structure is excited by incident transverse electromagnetic (TEM) waves traveling along the *x*-axis. The magnetic field (H-field) polarization occurs along the *y*-axis, whereas the electric field (E-field) polarization occurs along the *z*-axis. The proposed TCSRRs-MTM effective permittivity can be retrieved with the following equations, which are based on the results of the S-parameters ($S_{21}$ and $S_{11}$) [20]:

$$n = \frac{1}{kd} cos^{-1}\left[\frac{1}{2S_{21}}\left(1 - S_{11}^2 + S_{21}^2\right)\right] \tag{5}$$

$$z = \frac{\sqrt{(1 + S_{11})^2 - S_{21}^2}}{\sqrt{(1 - S_{11})^2 - S_{21}^2}} \tag{6}$$

$$\varepsilon = \frac{n}{z} \tag{7}$$

where $(n)$ represents the refractive index, (d) is the dielectric thickness, $(z)$ is impedance, $(\varepsilon)$ is the effective permittivity, (k) denotes the wave vector in free space, $(S_{11})$ is the reflection coefficient, and $(S_{21})$ is the transmission coefficient of the TCSRRs unit cell. The S-parameters ($S_{21}/S_{11}$) and the extracted components (real and imaginary) of the effective permittivity $(\varepsilon)$ for the TCSRRs-MTM unit cell structure are illustrated in Figure 3a,b, respectively.

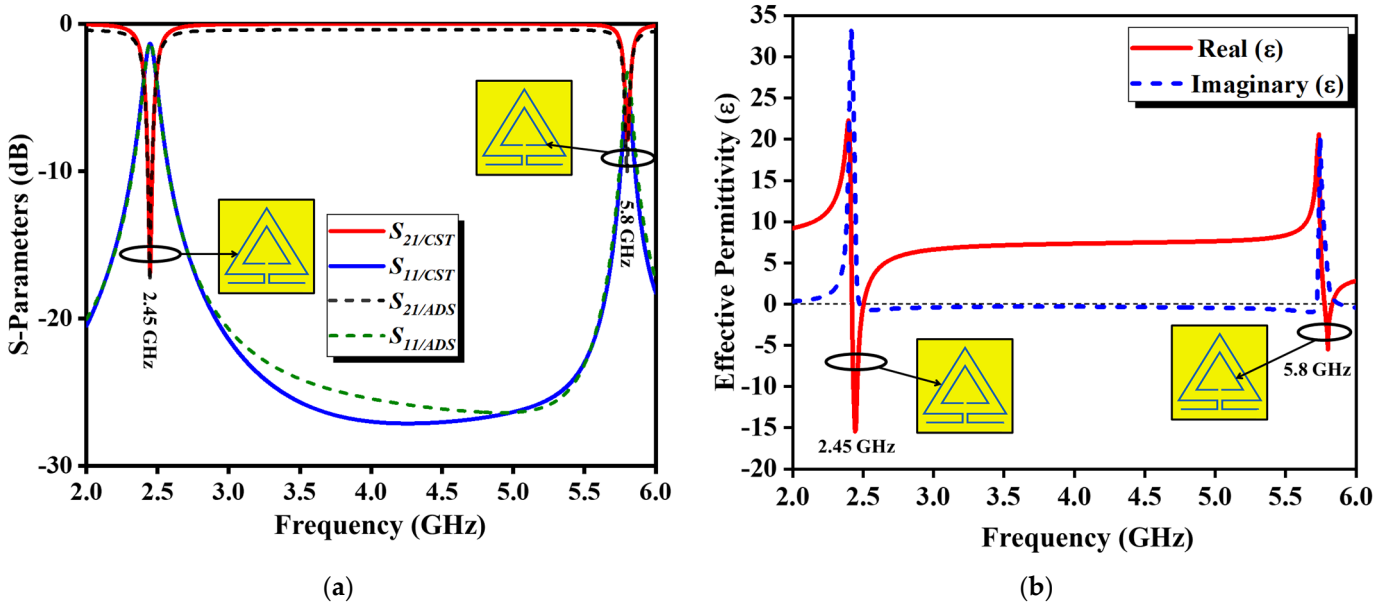


**Figure 3.** TCSRRs unit cell: (**a**) S-parameters and (**b**) the extracted effective permittivity ($\varepsilon$).

The structure of TCSRRs has two resonance frequencies at 2.45 and 5.8 GHz. The corresponding transmission coefficients are −15.5 and −5.5 dB, respectively, as depicted in Figure 3a. Furthermore, it is noticed that there is a significant agreement between the CST and ADS S-parameter results of the TCSRR unit cell. Figure 3b shows that the outer L-TCSRR structure has a negative permittivity at 2.45 GHz (−15.5), while the inner TCSRR has a negative permittivity at 5.8 GHz (−5.5). Table 1 summarizes the main characteristics of the TCSRRs-MTM unit cell structure.

**Table 1.** TCSRR-MTM structure characteristics.

| Unit Cell | Size ($mm^2$) ($\lambda_g{}^2$) | Frequency (GHz) | $S_{21}$ (dB) | Effective Permittivity Real (ε) |
|---|---|---|---|---|
| L-TCSRR | (14.5 × 14.5) (0.15 × 0.15) | 2.45 | −17.2 | −15.5 |
| TCSRR | (8.5×8.5) (0.08 × 0.08) | 5.8 | −10.1 | −5.5 |
| TCSRRs | (14.5 × 14.5) (0.15 × 0.15) | 2.45/5.8 | −17.2/10.1 | −15.5/−5.5 |

### *2.2. Proposed Antenna Geometry*

The proposed printed antenna comprises an apple-shaped radiator loaded with two triangular complementary split ring resonators (TCSRRs) printed on jeans fabric substrate material with 1.67 relative permittivity ($\varepsilon_r$), 0.0033 loss tangent ($\tan\delta$), and 2.84 mm in height ($h$). The printed antenna is fed using a coplanar waveguide (CPW) feeding method, which offers advantages such as low losses, coplanar nature, ease of fabrication, the capability to regulate characteristic impedance, and especially low radiation loss, which reduces the antenna-to-body coupling effect, making it more efficient for wearable antennas [21]. The inset-feed technique is also used to achieve a maximum 50 Ω impedance matching between the patch radiator and the microstrip feed line.

The TCSRR metamaterial structures are loaded on the patch antenna to achieve the desired frequency bands (2.45/5.8 GHz) while maintaining the compact antenna size. The proposed compactly printed antenna has a total size of 19.5 × 25 × 2.84 $mm^3$ (0.2 $\lambda_g$ × 0.26 $\lambda_g$ × 0.029 $\lambda_g$). The proposed antenna is designed and simulated in CST (Version 2023), ADS (Version 2021), and HFSS (Version 2023) software simulators, resonating at 2.45/3.5/5.8 GHz. The design evolution of the suggested printed antenna and its related reflection coefficient ($S_{11}$) results are illustrated in Figures 4a–d and 5, respectively.

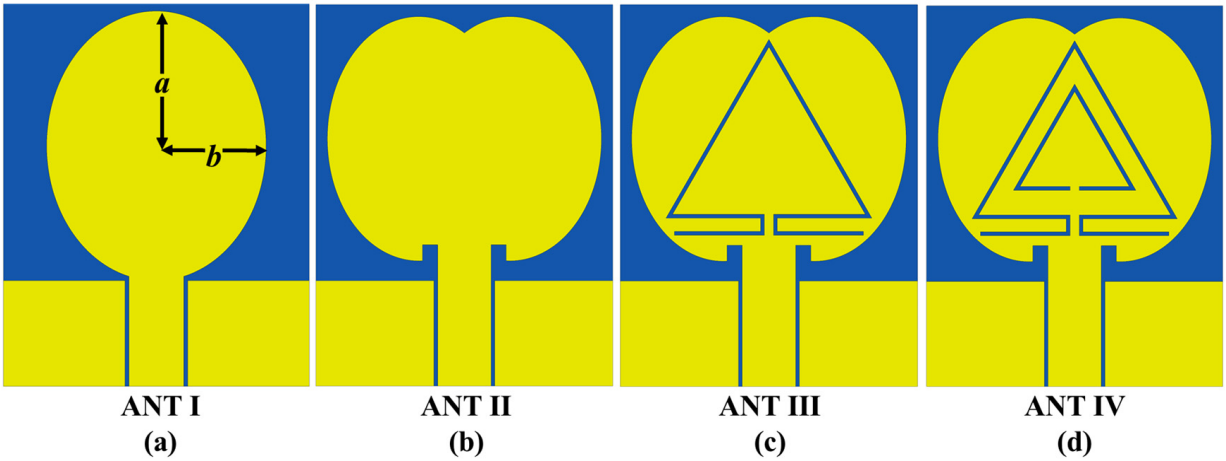


**Figure 4.** Proposed antenna design iterations process: (**a**) elliptical patch, (**b**) apple-shaped patch, (**c**) apple-shaped patch loaded with L-TCSRR, and (**d**) the final design of proposed antenna loaded with two TCSRRs.

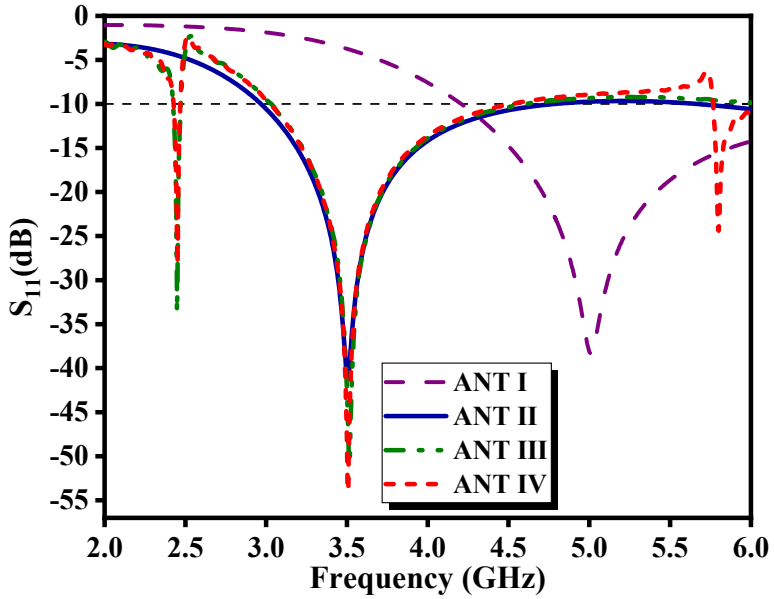


**Figure 5.** Reflection coefficient evolution with antenna design iterations.

The first step (ANT I) introduces a traditional CPW-fed elliptical printed antenna, as represented in Figure 4a. This antenna generates a resonance frequency at 5 GHz, as shown in Figure 5 (ANT I). The selection of the elliptical shape for the patch antenna was based on its flexibility compared to other typical designs such as square, rectangular, and circular patches [22]. The dimensions of the elliptical radiating patch are calculated using the following design equations [23,24]:

$$f_r = \frac{7.2}{\{(L + r + p) \times k\}} \tag{8}$$

where the lowest resonant frequency within the operating bandwidth is represented as $f_r$ (GHz), the height of the patch radiator is referred to as $L$ (cm), which is equivalent to a cylindrical monopole; the effective radius of an equivalent cylindrical monopole antenna is represented as $r$ (cm), and $p$ refers to the length of the feed line. Due to the presence of dielectric, the empirical value of 0.6 has been given to the factor $k$ for the jeans substrate. For an elliptical patch antenna, $L$ and $r$ are expressed based on the semimajor ($a$) and semi-minor ($b$) axes [23,24].

$$L = 2a, \quad r = \frac{b}{4} \tag{9}$$

The area of an elliptical patch is equal to the geometric mean of the areas of two circular patches with radii $a$ and $b$, respectively. This can be expressed mathematically as:

$$\pi ab = \sqrt{\pi a^2 \cdot \pi b^2} \tag{10}$$

The expression for the calculation of the effective semimajor axis $\left(a_{eff}\right)$, the semi-minor axis $\left(b_{eff}\right)$, and the resonant frequencies for an elliptical microstrip-printed antenna are given by [25,26]:

$$a_{eff} = a\left[1 + \frac{2h}{\pi\varepsilon_r a}\left\{\ln\frac{a}{2h} + (1.41\varepsilon_r + 1.77) + \frac{h}{a}(0.268\varepsilon_r + 1.65)\right\}\right]^{\frac{1}{2}} \tag{11}$$

$$b_{eff} = b\left[1 + \frac{2b}{\pi\varepsilon_r b}\left\{\ln\frac{b}{2h} + (1.41\varepsilon_r + 1.77) + \frac{h}{b}(0.268\varepsilon_r + 1.65)\right\}\right]^{\frac{1}{2}} \tag{12}$$

The resonant frequency is given as:

$$(f_r)_{11}^{e,o} = \frac{15}{\pi e a_{eff}} \sqrt{\frac{q_{11}^{e,o}}{\varepsilon_r}} \tag{13}$$

$$q_{11}^{e} = -0.0049e + 3.7888e^2 - 0.727e^3 + 2.314e^4 \tag{14}$$

$$q_{11}^{o} = -0.0063e + 3.8316e^2 - 1.1351e^3 + 5.2229e^4 \tag{15}$$

where $h$ represents the dielectric substrate thickness, $\varepsilon_r$ is the substrate relative permittivity, $e$ is the eccentricity of the elliptical patch, $a_{eff}$ is the effective length of the semimajor axis, $q_{11}^{e,o}$ is the dominant mode's Mathieu function ($TM_{11}^{e,o}$), and the dual resonant frequency is denoted by $(f_r)_{11}^{e,o}$.

In the second design step (ANT II), the patch radiator was formed as an apple shape by combining two ellipses of the patch and creating an inset-fed to the patch (Figure 4b), which shifted the resonance frequency towards the lower band (3.5 GHz) with a reflection coefficient below −40 dB, as illustrated in Figure 5 (ANT II). Next, an outer triangular CSRR connected with the L-slot at the end of its edges (Figure 4c) is loaded into the patch radiator. This allowed the antenna to generate a resonance frequency of 2.45 GHz while maintaining a compact size and preserving the main resonance frequency of the antenna (3.5 GHz), as shown in Figure 5 (ANT III).

Lastly, as presented in Figure 4d, an interior TCSRR is loaded into (ANT III) where the surface current distribution is less to obtain the third resonance frequency (5.8 GHz) without losing or affecting the previous frequencies of the antenna (2.45/3.5 GHz), as depicted in Figure 5 (ANT IV). The geometry of the proposed triple-band metamaterial-inspired printed antenna and its ECM are presented in Figure 6. The optimized antenna parameter dimension values are listed in Table 2.

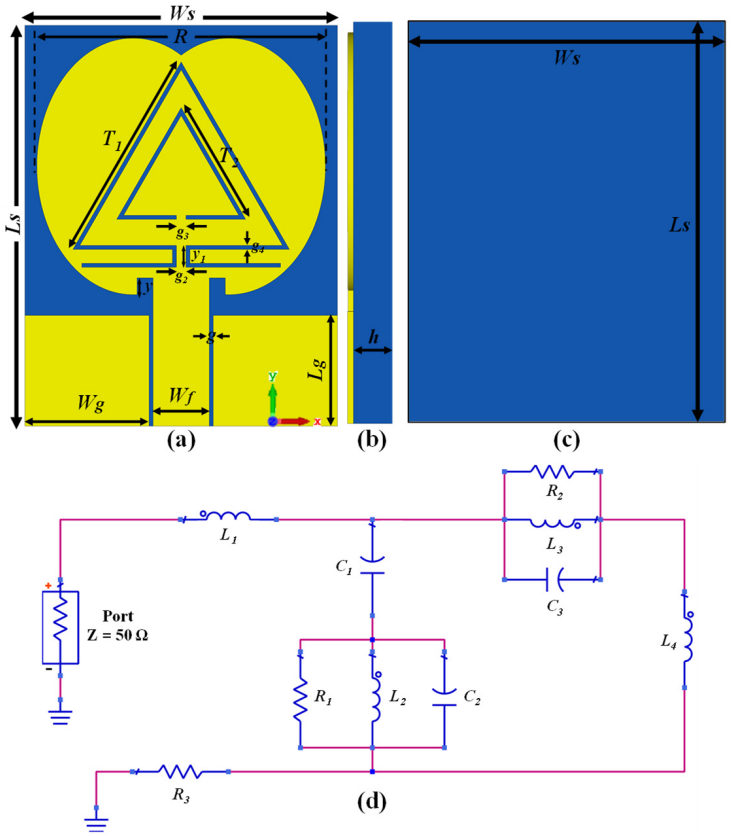


**Figure 6.** Proposed tri-band antenna geometry: (**a**) front view, (**b**) side view, (**c**) bottom view, and (**d**) ADS equivalent circuit model.

**Table 2.** The geometric parameters of the proposed printed antenna.

| Parameters | Value (mm) | Parameters | Value (mm) |
|---|---|---|---|
| $Ws$ | 19.5 | $a$ | 8 |
| $Ls$ | 25 | $b$ | 6 |
| $Wg$ | 7.85 | $g$ | 0.2 |
| $Lg$ | 6.9 | $g_2$ | 0.6 |
| $T_1$ | 13.5 | $g_3$ | 0.6 |
| $T_2$ | 8.5 | $g_4$ | 0.25 |
| $y$ | 1 | $R$ | 18 |
| $y_1$ | 1.2 | $Wf$ | 3.5 |

The proposed tri-band antenna's ECM is created and simulated using the Advanced Design System (ADS, Version 2021) software. It consists of two parallel RLC ($R_1L_2C_2$, $R_2L_3C_3$) circuits connected in parallel to each other and coupled with two inductors ($L_1$, $L_4$) and a capacitor ($C_1$), besides a resistor ($R_3$) to achieve impedance matching, as shown in Figure 6d.

A parallel RLC ($R_1L_2C_2$) circuit is used for the 2.45 GHz band. On the other side, another parallel RLC ($R_2L_3C_3$) circuit connected in series with an inductor ($L_4$) and a capacitor ($C_1$) is used to generate the middle (3.5 GHz) and high-frequency (5.8 GHz) bands. The impedance matching of the ECM can be optimized by varying the resistor values, while the $S_{11}$ can be tuned by changing the capacitor values ($C_1$, $C_2$, $C_3$) and inductors ($L_1$, $L_2$, $L_3$, $L_4$). The lumped component values of ECM are summarized in Table 3.

**Table 3.** Antenna ECM lumped element values.

| Inductors | Value (nH) | Capacitors | Value (pF) | Resistors | Value (Ω) |
|---|---|---|---|---|---|
| $L_1$ | 2.25 | $C_1$ | 1.12 | $R_1$ | 7906 |
| $L_2$ | 0.1 | $C_2$ | 38.27 | $R_2$ | 5000 |
| $L_3$ | 1.64 | $C_3$ | 1.09 | $R_3$ | 50 |
| $L_4$ | 2.17 | $C_{L\text{-}TCSRR}$ | 25.72 | | |
| $L_{L\text{-}TCSRR}$ | 0.16 | $C_{TCSRR}$ | 19.75 | | |
| $L_{TCSRR}$ | 0.04 | | | | |

The comparison in Figure 7 demonstrates a strong agreement between CST MWS, ANSYS HFSS, and ADS for the reflection coefficient ($S_{11}$). However, there is a slight shift in the middle-frequency band (3.5 GHz) due to variations in the numerical computation methods used by CST and HFSS. Table 4 presents the summary results of the comparative performance analysis of the presented antenna using CST, HFSS, and ADS simulation tools.

**Table 4.** Comparative summary of antenna performance in CST, HFSS, and ADS.

| Frequency (GHz) | CST | | HFSS | | ADS | |
|---|---|---|---|---|---|---|
| | BW (MHz) FBW (%) | $S_{11}$ (dB) | BW (MHz) FBW (%) | $S_{11}$(dB) | BW (MHz) FBW (%) | $S_{11}$ (dB) |
| 2.45 | 50<br>2.05 | −28.19 | 50<br>2.05 | −23.94 | 60<br>2.47 | −40.5 |
| 3.5 | 1530<br>44.3 | −53.93 | 1800<br>51.45 | −27.86 | 1180<br>33.8 | −48.22 |
| 5.8 | 240<br>4.65 | −24.4 | 240<br>4.15 | −38.9 | 290<br>5.19 | −34.82 |

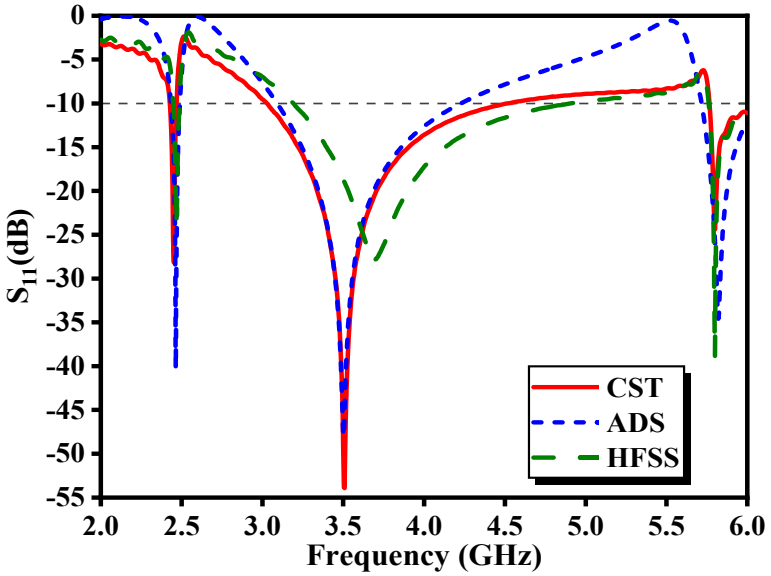


**Figure 7.** Proposed antenna reflection coefficient ($S_{11}$) in CST, ADS, and HFSS.

Figure 8 depicts the surface current distribution for the proposed printed antenna at 2.45/3.5/5.8 GHz. At the lower band, the most current flows around the outer L-TCSRR in the radiating patch, which is connected with the L-slot at the end of its edges, while at the middle band (3.5 GHz), the current is mainly concentrated in the microstrip feed line, radiating element edges, and CPW feed.

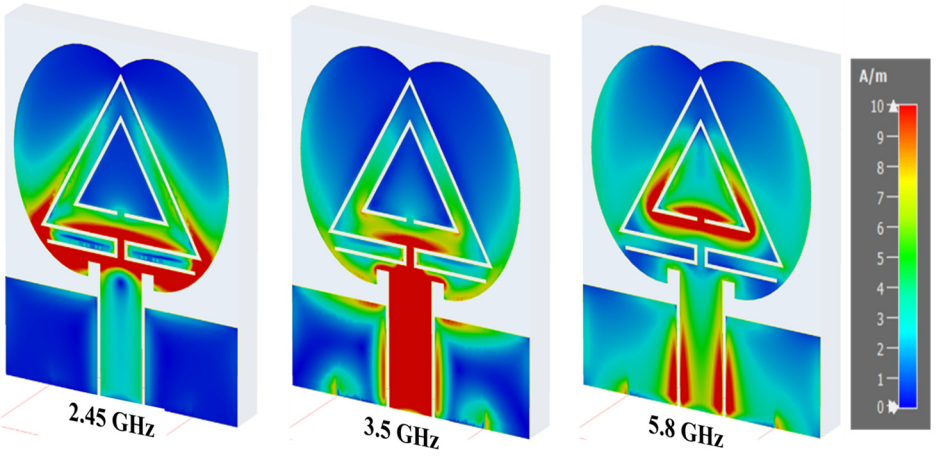


**Figure 8.** Current antenna distribution at operating frequencies.

At 5.8 GHz, the current is distributed around the inner TCSRR in the radiating patch, and some of the current flows at the edges of the feed line and CPW feed, as shown in Figure 8. We conclude that the outer L-TCSRR structure produces the maximum current at 2.45 GHz. On the other hand, the inner TCSRR structure generates the maximum current at 5.8 GHz, based on Figure 8.

## 3. Design and Characteristics Analysis of UC-EBG

There are various planar EBG configurations, but the two primary ones are the uni-planar compact electromagnetic bandgap (UC-EBG) and mushroom EBG. The UC-EBG is preferred for wearable antennas due to its compact size, simplicity (no vias are required), low cost, and compatibility with planar circuits [5,27]. Several UC-EBG structures have been created to increase bandgap width and reduce periodic size [15,28–30].

The proposed UC-EBG structure is shown in Figure 9a,b, with overall dimensions of $13 \times 13 \times 2.84$ mm$^3$ ($0.13\ \lambda_g \times 0.13\ \lambda_g \times 0.029\ \lambda_g$). It is printed on jeans material with the same proposed antenna substrate properties. Figure 9c depicts the equivalent circuit model (ECM) of the proposed UC-EBG structure, which consists of three parallel LC circuits ($L_3C_3$, $L_4C_4$, and $L_5C_5$) connected in series with two inductors ($L_1$, $L_2$) and two capacitors ($C_1$, $C_2$). The ECM is designed using transmission-line theory.

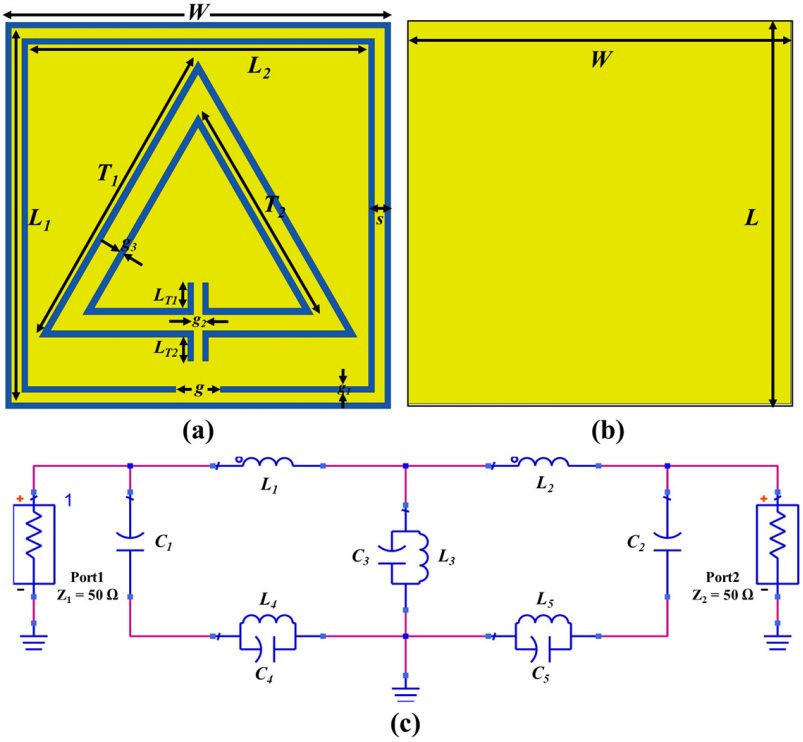


**Figure 9.** Proposed UC-EBG design geometry: (**a**) front view, (**b**) back view, and (**c**) ECM.

The following equation can be used to estimate the resonant frequency ($f_r$) of the proposed UC-EBG unit cell in terms of the equivalent circuit model elements [31]:

$$f_r = \frac{1}{2\pi\sqrt{L_T C_T}} \tag{16}$$

where $C_T$ and $L_T$ represent the total equivalent capacitance and inductance for each resonant frequency in the ECM of the UC-EBG structure.

Generally, the unit cell length of the EBG structure should be less than $\lambda/2$ of the lowest resonant frequency, which in our study was found to be 61 mm at 2.45 GHz. By the incorporation of metamaterial structures, such as the Rectangular Complementary Split Ring Resonator (RCSRR) and the Modified Triangular Complementary Split Ring Resonator (M-TCSRR), into the UC-EBG structure and through the optimization of the inter-resonator gap distances, the capacitance of the UC-EBG structure can be significantly enhanced; thus, a 79% reduction in size is achieved in comparison to traditional EBG structures. This enhancement in compactness demonstrates the potential for more efficient and versatile electromagnetic structures in future applications. The optimized dimensions of the UC-EBG and the values of its ECM's lumped components in ADS are summarized in Tables 5 and 6, respectively.

**Table 5.** UC-EBG unit cell optimized dimensions summary.

| Parameters | Value (mm) | Parameters | Value (mm) |
|---|---|---|---|
| $W = L$ | 13 | $L_{T2}$ | 0.66 |
| $L_1$ | 12.7 | $g$ | 1.5 |
| $L_2$ | 11.5 | $g_1$ | 0.2 |
| $T_1$ | 10.74 | $g_2$ | 0.35 |
| $T_2$ | 7.79 | $g_3$ | 0.2 |
| $L_{T1}$ | 0.79 | $s$ | 0.3 |

**Table 6.** UC-EBG ECM lumped element values.

| Inductors | Value (nH) | Capacitors | Value (pF) |
|---|---|---|---|
| $L_1$ | 0.01 | $C_1$ | 1.03 |
| $L_2$ | 2.74 | $C_2$ | 0.64 |
| $L_3$ | 0.3 | $C_3$ | 3.82 |
| $L_4$ | 0.61 | $C_4$ | 1.84 |
| $L_5$ | 1.8 | $C_5$ | 1.07 |

This study examines two methods to analyze the band gap properties of the proposed UC-EBG structure at the desired operating frequencies: suspended transmission and dispersion diagram analysis [27].

### *3.1. Electromagnetic Bandgap Array (Suspended Line Method)*

Figure 10 depicts the two-port transmission line techniques that are used to attain the transmission coefficient of the EBG surface. In this configuration, the excitation source is on the left port, while the matching load is on the right port. The UC-EBG structure layer consists of nine elements arranged in a 3 × 3 UC-EBG array, with a total size of $39 \times 39 \times 2.84$ mm$^3$.

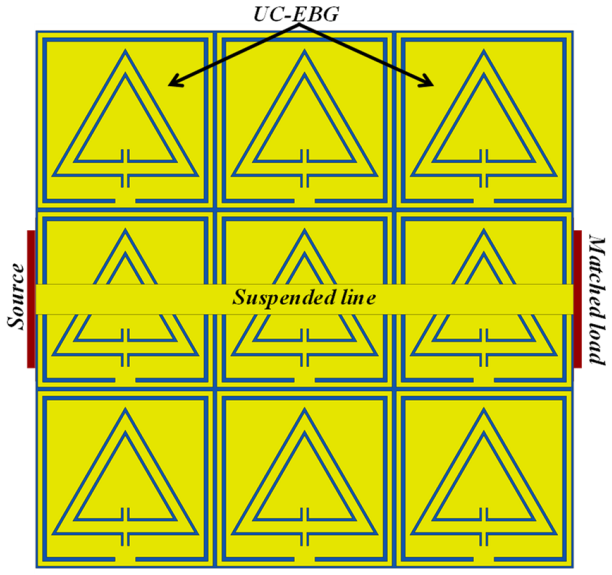


**Figure 10.** Suspended microstrip line method.

The transmission coefficient ($S_{21}$) of the UC-EBG array is shown in Figure 11. It is noted that the UC-EBG structure exhibits four peaks ($S_{21} < -10$ dB) at 2.45 GHz (2–2.85 GHz), 3.5 GHz (3.45–3.53 GHz), 4.9 GHz (4.85–4.94 GHz), and 5.8 GHz (5.65–6 GHz), indicating that the UC-EBG has four bandgaps in these frequency ranges, which can efficiently suppress surface waves.

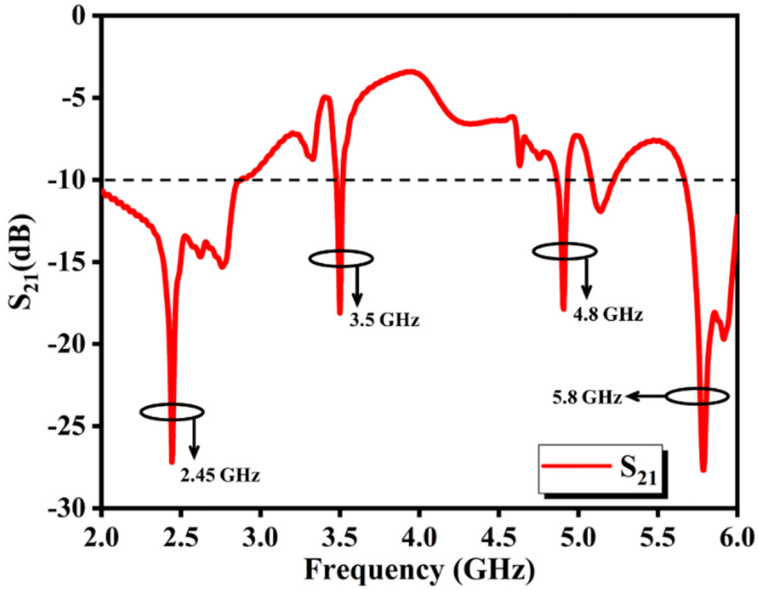


**Figure 11.** Transmission coefficient of a 3 × 3 UC-EBG array.

*3.2. Dispersion Diagram Method*

The dispersion diagram is a graphical representation of the frequency versus phase constant β (or propagation constant) of electromagnetic waves propagating through an EBG structure [5]. It is a helpful tool for analyzing the EBG structure and clearly shows the allowed and forbidden frequency ranges for electromagnetic waves. In the banned frequency range, the modes will not be excited, which means no waves can propagate within the band gap. This implies that the EBG structure suppresses the surface waves by reflection or absorption within a specific frequency range.

In CST MWS, the Eigenmode solver is used to plot the dispersion diagram (no source excitations are required, and the electric field direction is normal to the unit cell surface). The periodic boundaries are set for the side walls (X and Y directions) of the UC-EBG unit cell (the Eigenmode solver in CST does not support the open boundaries) and for the electric conductor, or PEC (Et = 0), in the Z directions, as shown in Figure 12a. The dispersion diagram of the proposed UC-EBG unit cell structure is shown in Figure 12b.

The representation of all possible propagation directions in the x and y directions can be combined into an irreducible Brillouin zone (Γ–X–M–Γ) [32], as indicated in Figure 12b, for the Brillouin zone. The dispersion diagram consists of three path sections, and each path has a unique phase shift achieved by moving along the boundary of the irreducible Brillouin zone.

In the first path (Γ–X), the phase along the x-axes is shifted from 0° to 180°, while the boundary phase shift along the *y*-axis is fixed at 0°. Then, in the second path (X–M), the *x*-axis boundary phase shift is fixed at 180°, and the *y*-axis boundary phase is shifted from 0° to 180°. In the last path (M–Γ), both the *x*-axis and *y*-axis boundaries phase shift simultaneously from 180° to 0°.

Dispersion diagrams usually include a light line, which represents the propagation behavior of light in (Γ–X) and (M–Γ) directions in the vacuum. The light line helps to define the guided and unguided propagating frequency modes. If a mode is below the light line, it is guided, and if it is above the light line, it is considered an unguided or leaky wave. The intersections with the light lines determine the maximum bandgap limit for the surface waves.

Four frequency Eigenmodes are used to determine the dispersion diagram of the proposed UC-EBG structure, which exhibits three bandgaps: (2.4 GHz to 3.6 GHz), (3.97 GHz to 5.1 GHz), and (5.4 GHz to 5.85 GHz), as illustrated in Figure 12b. These bandgaps correspond to the results of previous characteristic methods, which showed bandgaps at

2.45/3.5/5.8 GHz. Thus, the desired frequency bands are covered by all three characteristic methods.

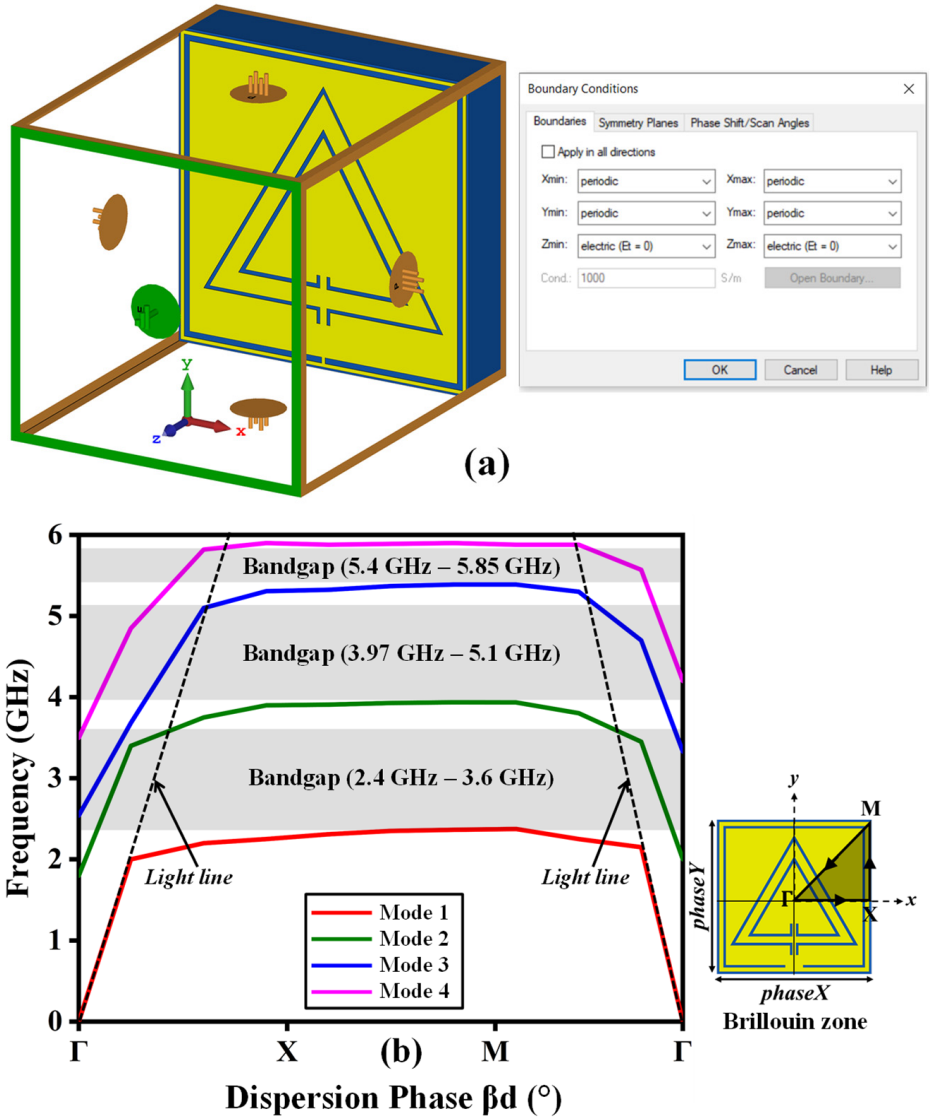


**Figure 12.** (**a**) Periodic boundary conditions and (**b**) dispersion diagram of the UC-EBG structure.

Table 7 presents a comparative summary between the proposed UC-EBG unit cell and various recent compact EBG unit cells. The integration of TCSRR metamaterials in the proposed UC-EBG unit cell has resulted in a significant size reduction, with dimensions of 13 mm × 13 mm, compared to the EBG unit cells discussed in Table 7.

Despite its compact size, the UC-EBG unit cell operates within a frequency range of 2.45/3.5/5.8 GHz, which is crucial for versatile applications. The utilization of advanced characterization techniques, such as suspended line and dispersion diagram techniques, ensures accurate analysis of the UC-EBG performance. Therefore, incorporating TCSRR metamaterials in the UC-EBG design has successfully led to a superior compact EBG structure that maintains its operational capabilities.

The design methodology for the proposed tri-band wearable antenna backed by a UC-EBG structure is depicted in Figure 13. This chart outlines the process used to design the proposed wearable textile antenna with UC-EBG structure in this research paper.

**Table 7.** Recent compact EBG structure comparisons.

| Ref. | Year | EBG Type | EBG Unit-Cell Size ($mm^2$) | Operating Frequency (GHz) | EBG Characterizations Methods |
|---|---|---|---|---|---|
| [33] | 2023 | EBG-AMC (Cross-shape) | 24.6 × 24.6 | 2.45 | Reflection phase |
| [34] | 2023 | EBG-AMC (Circular-ring) | 25.5 × 25.5 | 2.45/5.8 | Reflection phase |
| [9] | 2022 | MEBG (Mushroom-like EBG) | 29 × 29 | 2.45/5.4 | Reflection phase and suspended line |
| [11] | 2021 | EBG (Rectangular-stubs) | 40.6 × 40.6 | 2.45/3.5/5.8 | Suspended line |
| [35] | 2019 | EBG-AMC (Single SRR) | 30 × 30 | 2.45 | Reflection phase and suspended line |
| [36] | 2018 | EBG (Rectangular-ring patch) | 27 × 27 | 2.45 | Reflection phase |
| This work | / | UC-EBG-AMC (TCSRRs-MTM) | 13 × 13 | 2.45/3.5/5.8 | Suspended line and dispersion diagram |

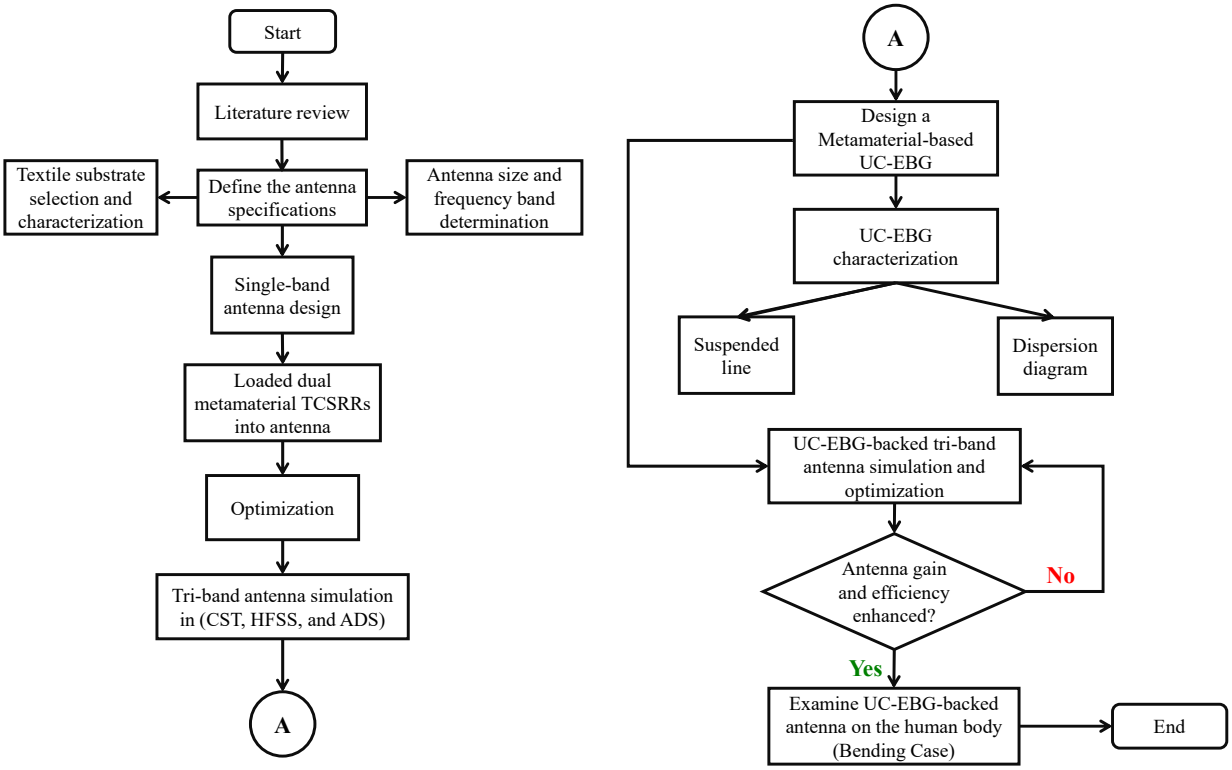


**Figure 13.** Design methodology flowchart for the proposed UC-EBG-backed tri-band wearable textile antenna.

## 4. Analysis of The Tri-Band Antenna Backed by UC-EBG in Free Space

A 3 × 3 UC-EBG array is employed as a ground plane to enhance the gain and efficiency of the proposed printed antenna, as depicted in Figure 14. The compact CPW-fed tri-band antenna is placed above the UC-EBG layer with a 1 mm thick foam selected for optimal performance. Using foam allows us to place the antenna on the UC-EBG plane without any impact on the antenna's performance.

Figure 15 compares the simulated $S_{11}$ result of the tri-band antenna with and without the UC-EBG plane. Excellent impedance matching ($S_{11} < -20$ dB) is achieved by the proposed antenna with a 3 × 3 UC-EBG layer at the resonant frequencies (2.45/3.5/5.8 GHz), except for the parasitic frequency (~5 GHz).

The coupling between the 3 × 3 UC-EBG layer and the antenna resulted in a narrower bandwidth than the one without UC-EBG, especially at 3.5 GHz. However, this work aims to safeguard the human body from harmful antenna radiation by reflecting it toward the intended beam direction and improving the antenna gain via the UC-EBG layer at the desired frequencies.

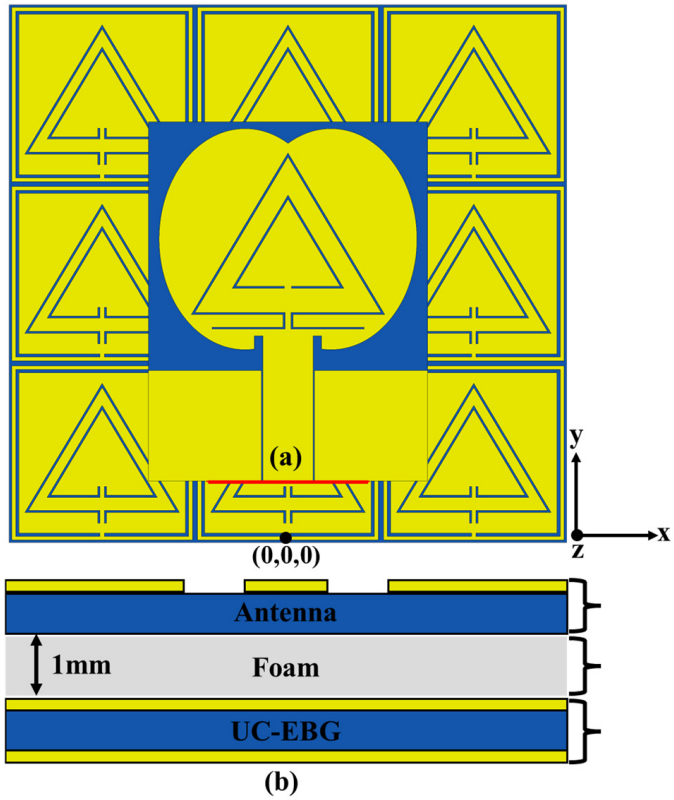


**Figure 14.** Proposed antenna on the UC-EBG plane in free space: (**a**) front view and (**b**) side view.

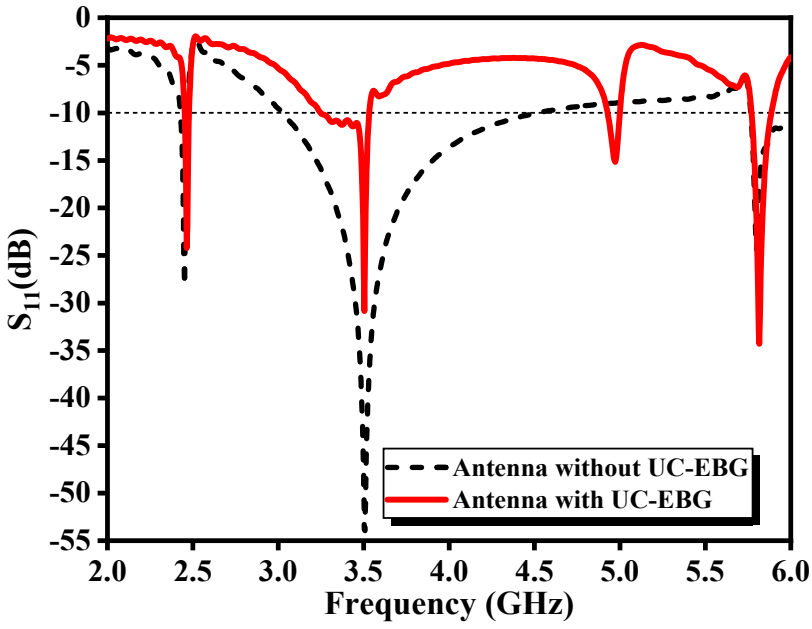


**Figure 15.** $S_{11}$ comparison of the tri-band antenna with and without UC-EBG in free space.

Antenna deformation integrated into wearable devices is anticipated in WBAN applications, especially when worn in different positions on the human body. Therefore, the antenna with UC-EBG is bent at different deformations to examine and ensure the consistency of its performance in free space before being loaded onto a human body. Bending examinations of the UC-EBG-backed antenna are conducted and evaluated in CST MWS on a vacuum model with different radii (20 mm, 40 mm, 60 mm, and 80 mm) along the x- and y-axes, as shown in Figure 16. These radii are selected based on the approximate size of an

adult and child's arm and leg, with an extra 20 mm added for the worst-case scenario of antenna bending. The $S_{11}$ of the proposed UC-EBG-backed antenna with varying bending radii (r) along the x- and y-axes is compared in Figure 17a,b.

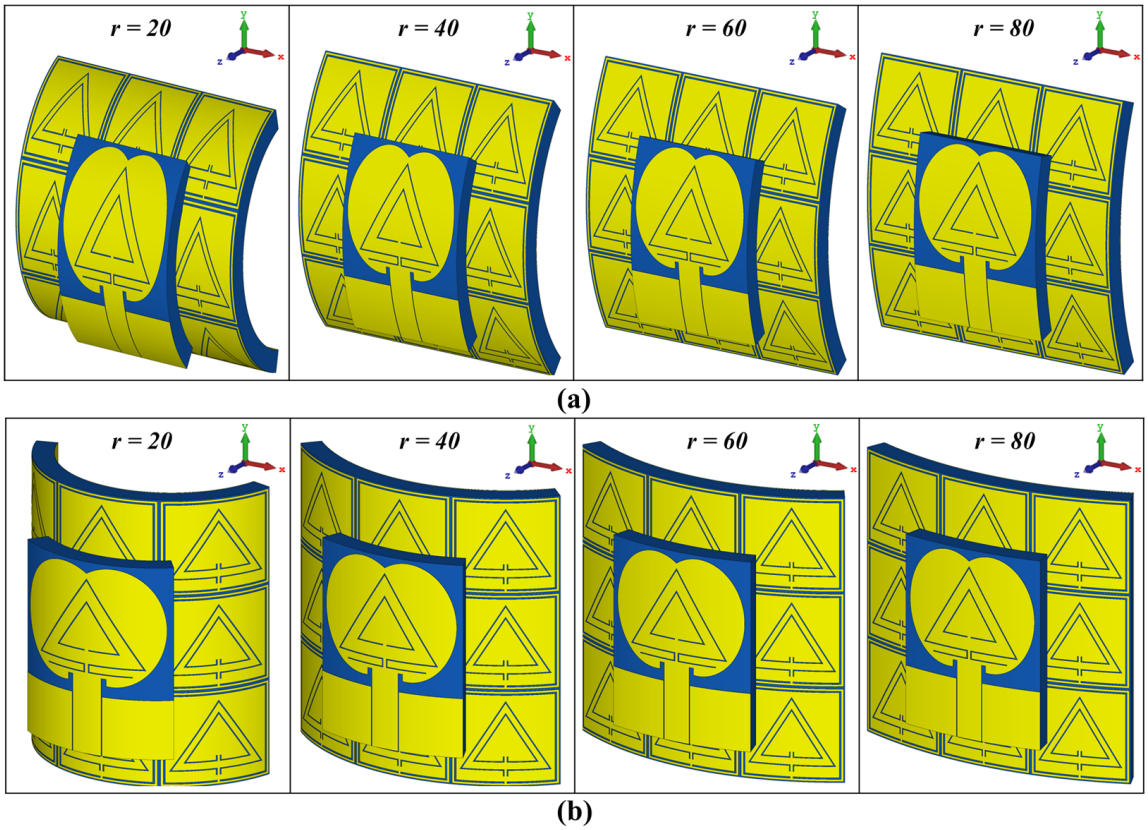


**Figure 16.** Bending process of the UC-EBG-backed antenna in free space at different radii along (**a**) the *x*-axis and (**b**) the *y*-axis.

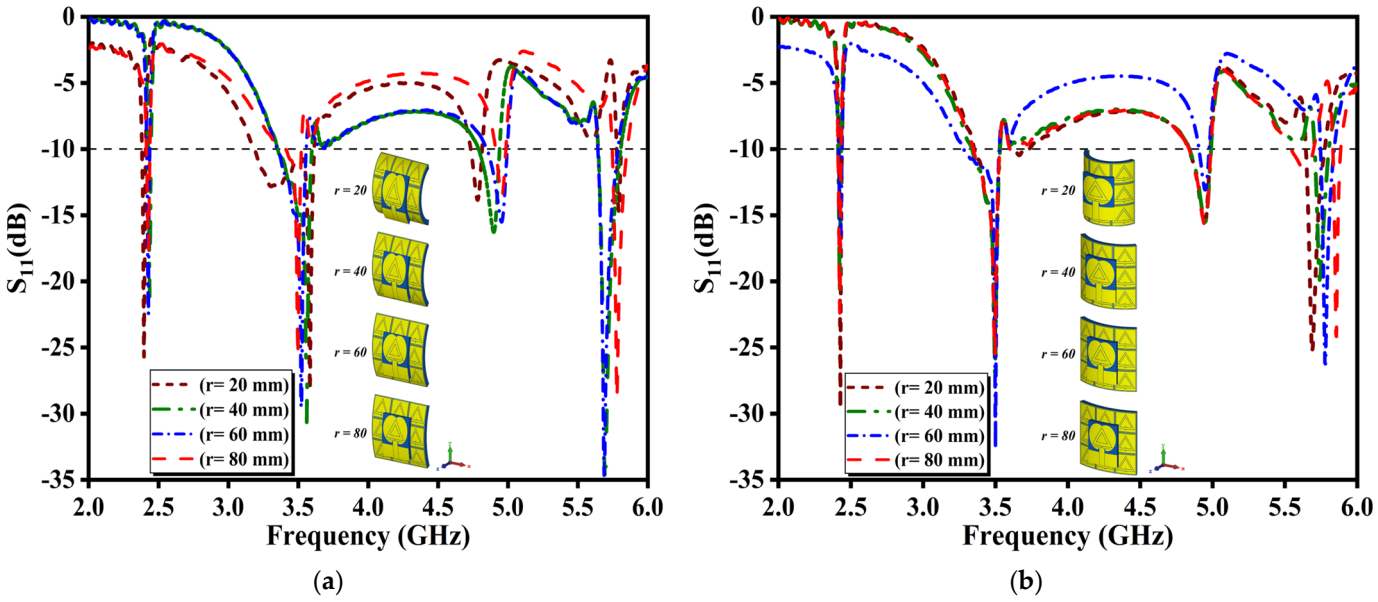


**Figure 17.** $S_{11}$ of the UC-EBG-backed proposed antenna under bending effect in free space at various radii across (**a**) the *x*-axis and (**b**) along the *y*-axis.

The proposed wearable antenna with the UC-EBG layer indicates better impedance matching ($S_{11} < -15$ dB) at the operating frequencies for all radii values along the *x*-axis and *y*-axis. However, it is worth mentioning that bending the antenna along the *x*-axis causes a slight shift in resonant frequencies (Figure 17a). Along the *y*-axis, the antenna produces a minor shift from the higher band toward the lower band (Figure 17b). As the radius of the curvature decreases (the degree of bending increases), the bending effect becomes more noticeable. Nevertheless, the bandwidth for each resonant frequency remains constant under all conditions. The proposed UC-EBG-backed antenna has generally demonstrated adaptability and robustness under various curvature conditions.

## 5. Human-Proximity UC-EBG-Backed Antenna (On-Body Curvature Analysis)

After examining the bending effect of the proposed antenna with the UC-EBG plane in free space, this section will investigate the impact of the UC-EBG-backed antenna bending on its performance when placed on the curved parts of the human body. The UC-EBG-backed antenna is bent around three model cases of curved body parts: a child's arm (worst case) with a 40 mm radius, an adult's arm with a 60 mm radius, and an adult's leg with a 70 mm radius, as shown in Figure 18.

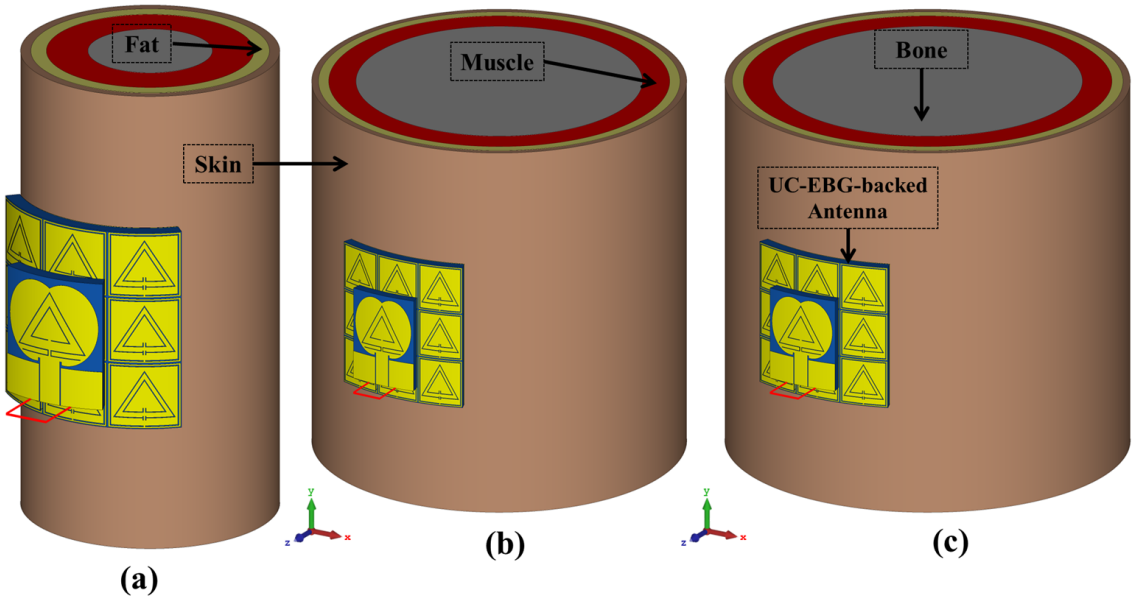


**Figure 18.** The proposed antenna with the UC-EBG plane is placed and bent around three model cases of curved human body parts: (**a**) child arm (worst case: r = 40 mm), (**b**) human arm (r = 60 mm), and (**c**) human leg (r = 70 mm).

In order to examine the compatibility of the proposed antenna with the UC-EBG layer for WBAN applications, the SAR is calculated when the UC-EBG-backed antenna is proximal to a human body using a human body phantom model. The UC-EBG structure is used as the antenna ground plane to minimize the back radiation towards the human body and, therefore, decrease the SAR value to make the antenna suitable for WBAN applications. The antenna, with and without UC-EBG, is placed 1 mm away from the human phantom model to examine its effect on the human body. The values for mass density, thickness, electrical conductivity, and permittivity for each tissue layer are tabulated in Table 8.

**Table 8.** Properties of human tissue layers [37].

| Layers \ Properties | Permittivity | Electrical Conductivity (S/m) | Density (kg/m$^3$) | Thickness (mm) |
|---|---|---|---|---|
| Skin | 36.703 | 2.041 | 1001 | 2 |
| Fat | 5.135 | 0.184 | 900 | 3 |
| Muscle | 50.873 | 3.066 | 1006 | 10 |
| Bone | 10.615 | 0.721 | 1008 | 20 |

Figure 19 shows the $S_{11}$ comparison of the UC-EBG-backed antenna in free space and on the body tissues, which are significantly matched. The UC-EBG-backed antenna on the body tissues operates at 2.45 GHz in the lower band (2.44–2.47 GHz), 3.5 GHz in the middle band (3.19–3.95 GHz), and 5.8 GHz in the upper band (5.69–5.88 GHz). The contact between the antenna and human skin changes its permittivity, resulting in a minor shift at 2.45 GHz and a wider bandwidth at 3.5 GHz, which modifies its performance.

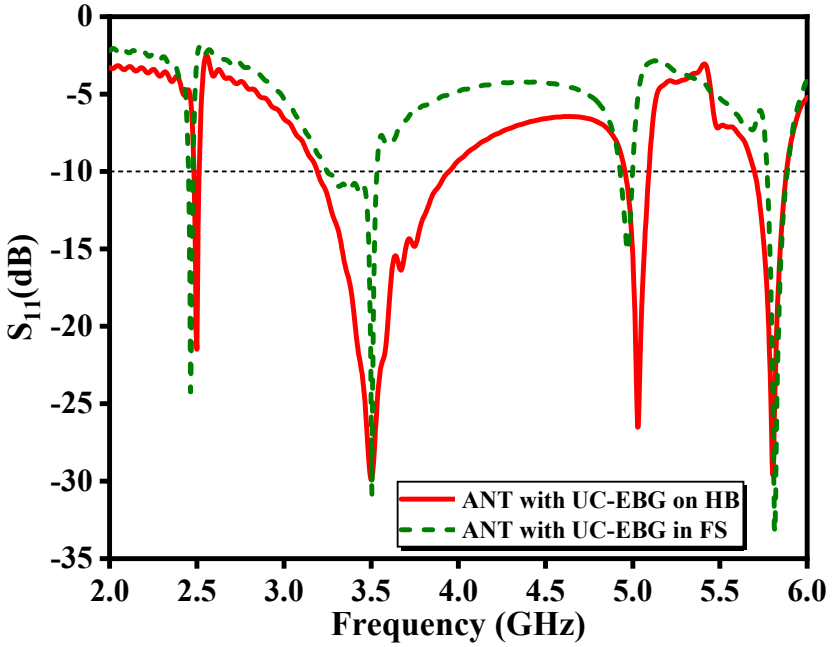


**Figure 19.** $S_{11}$ of the UC-EBG-backed antenna on the human body (HB) and in free space (FS).

The proposed compact tri-band textile antenna with UC-EBG can maintain adequate bandwidth across all three cases ($S_{11} < -10$ dB) while effectively covering the intended frequency range. This makes it suitable for wearable applications, as it can maintain optimal performance even when bent.

Figure 20 shows the 3D gain patterns of the proposed triple-band antenna with and without incorporating the UC-EBG structure across different physical bending conditions to simulate its performance on different human body parts. The 3D radiation patterns are simulated at 2.45, 3.5, and 5.8 GHz, and the evaluated conditions included a child's arm, an adult's arm, and an adult's leg with a radius of 40 mm, 60 mm, and 70 mm, respectively.

It has been shown that the presence of the UC-EBG structure improves the antenna gain by controlling and concentrating its radiation pattern on the main lobe, thus reducing the backward radiation. This improvement is due to the UC-EBG structure's ability to maintain the antenna's radiation pattern even when the antenna is bent to conform to the curvature of the body part.

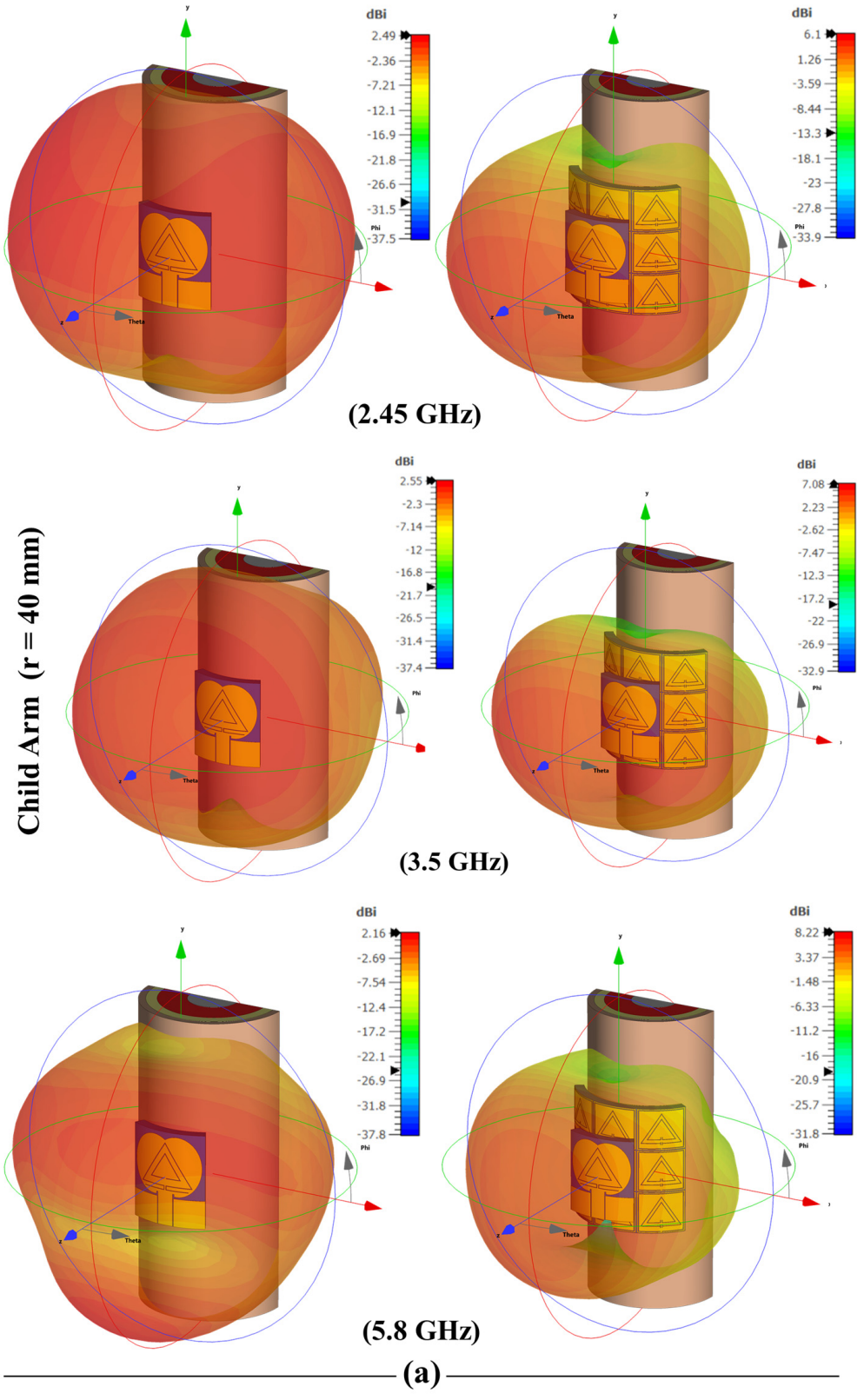


**Figure 20.** *Cont.*

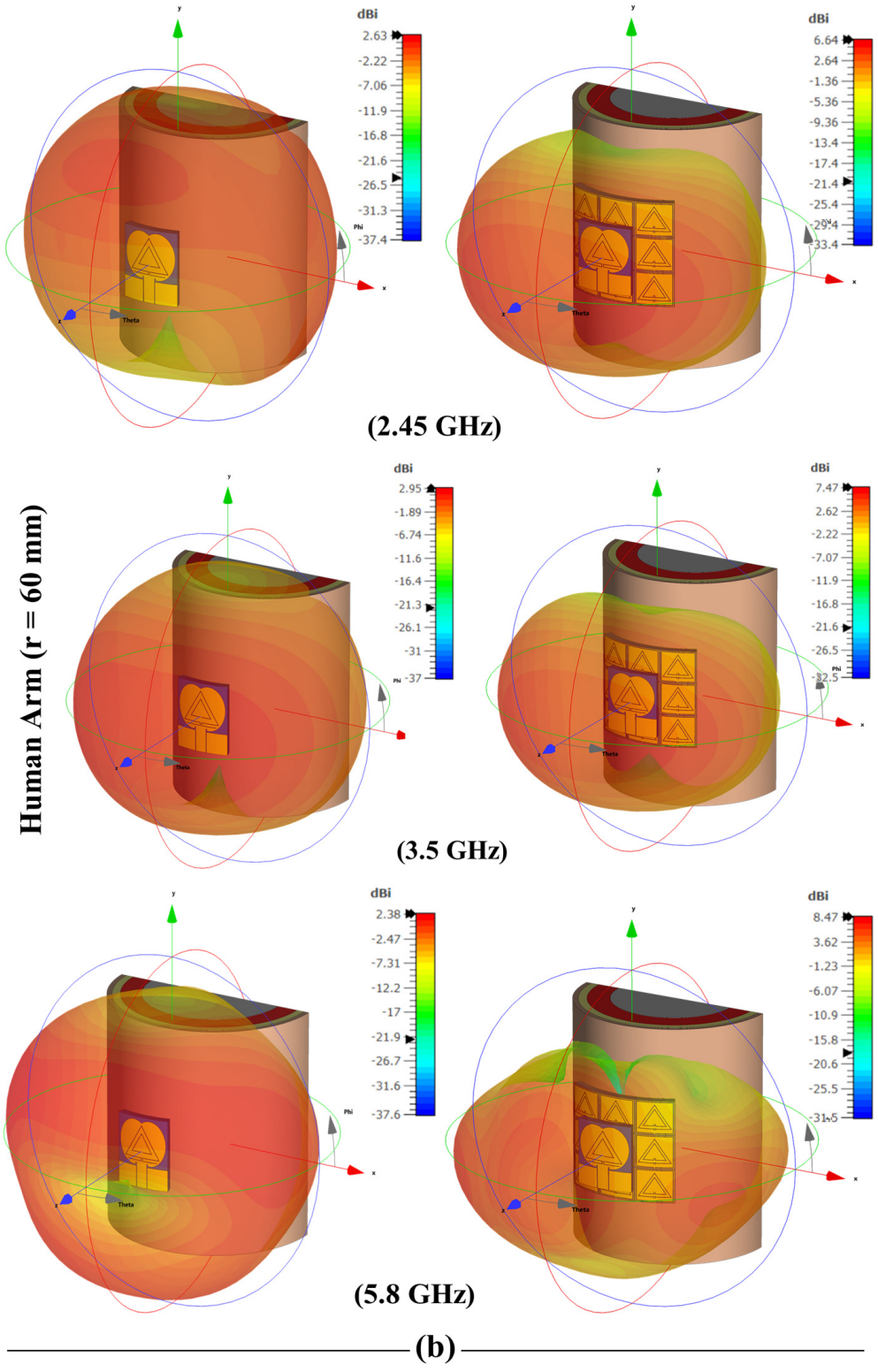


**Figure 20.** *Cont.*

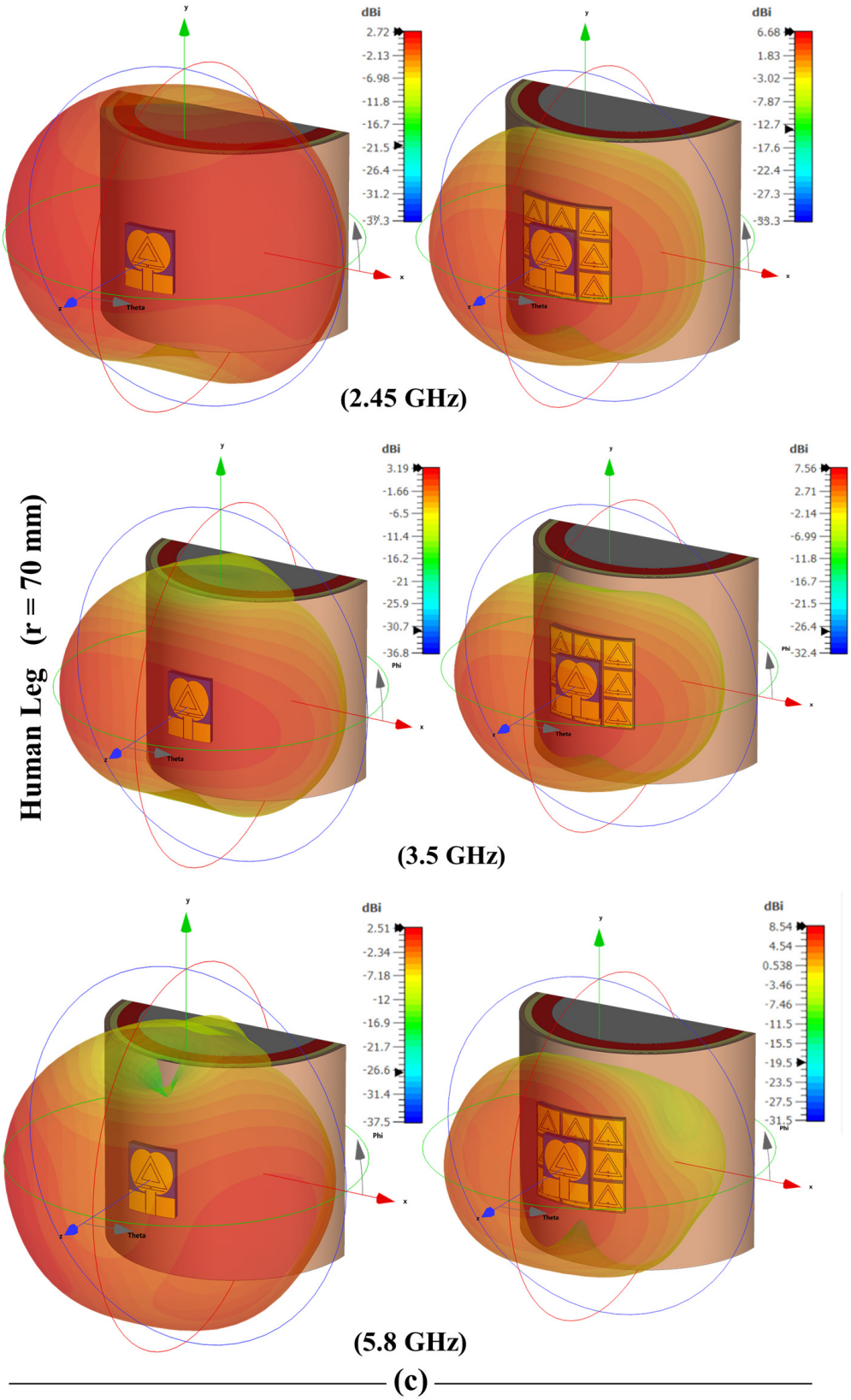


**Figure 20.** Three-dimensional-gain pattern of the proposed antenna under different bent conditions on the human body in the presence and absence of the UC-EBG layer: (**a**) child arm (r = 40 mm), (**b**) adult arm (r = 60 mm), and (**c**) human leg (r = 70 mm).

Table 9 outlines the performance comparison of the proposed antenna with and without UC-EBG in various scenarios at 2.45, 3.5, and 5.8 GHz.

**Table 9.** Performance comparison of the antenna with and without UC-EBG in different scenarios.

| Scenarios | Frequency (GHz) | Gain (dBi) | Directivity (dBi) | Efficiency (%) |
|---|---|---|---|---|
| Antenna without UC-EBG | 2.45 | 2.49 | 5.47 | 50.49 |
| | 3.5 | 2.55 | 5.39 | 51.98 |
| | 5.8 | 2.16 | 5.83 | 43.05 |
| Antenna with UC-EBG (40 mm) | 2.45 | 6.1 | 7.08 | 79.83% |
| | 3.5 | 7.08 | 7.7 | 86.64% |
| | 5.8 | 8.22 | 8.89 | 85.93% |
| Antenna with UC-EBG (60 mm) | 2.45 | 6.64 | 7.54 | 80.81% |
| | 3.5 | 7.47 | 8.28 | 82.92% |
| | 5.8 | 8.47 | 9.14 | 85.79% |
| Antenna with UC-EBG (70 mm) | 2.45 | 6.68 | 7.6 | 80.8% |
| | 3.5 | 7.56 | 8.44 | 81.83% |
| | 5.8 | 8.54 | 9.35 | 83.59% |

## 6. Specific Absorption Rate (SAR) Analysis

Wearable antennas are made for on-body communications, which require the antenna to operate in close proximity to the human body. However, exposure to electromagnetic radiation may pose potential health risks to humans, especially when antennas are placed on the human body. Therefore, the SAR is used as a vital indicator parameter to measure the quantity of radiofrequency (RF) electromagnetic energy absorption per tissue mass of the human body, which can be calculated as follows [38]:

$$SAR = \frac{\sigma|E^2|}{\rho}[\mathrm{W/kg}] \tag{17}$$

where $E$ is the magnitude of the induced electric field (V/m) in the human body, and $\sigma$ and $\rho$ represent the electrical conductivity (S/m) and mass density (kg/m$^3$) of the biological human tissue, respectively.

The conductivity of tissues that absorb radiation is directly related to SAR and is inversely proportional to tissue density. Meanwhile, the electric field intensity is proportional to the power density of an electromagnetic wave [39].

$$Power = \frac{(E(V/m))^2}{377}\left[\mathrm{W/m^2}\right] \tag{18}$$

The CST MWS simulator software (Version 2023) is used to calculate the SAR using the IEEE C95.3 averaging method with 100 mW antenna input power [9]. Figure 21 displays the SAR values for the UC-EBG-backed antenna on different curved human body parts, including a child's arm (40 mm radius), an adult's arm (60 mm radius), and an adult's leg (70 mm radius), respectively. The SAR values are calculated at 2.45/3.5/5.8 GHz for tissue over 1 g and 10 g. The high-impedance surface of UC-EBG limits surface wave propagation, reflecting more energy and thus isolating the human body from antenna backward radiation, resulting in low SAR values.

Table 10 shows that the SAR values of the UC-EBG-backed wearable antenna on the human body at the resonant frequencies in bending scenarios are below the maximum SAR-limit safety standards set by the Federal Communications Commission (FCC) and Innovation, Science, and Economic Development (ISED) for 1 g of tissue (i.e., 1.6 W/kg) and over 10 g of tissue (i.e., 2 W/kg) recommended by the International Commission on Non-Ionizing Radiation Protection (ICNIRP) for European Standards. The UC-EBG layer

acts as a reflector of electromagnetic radiation, thus isolating and protecting the human body from exposure to harmful residual backward radiation from the antenna.

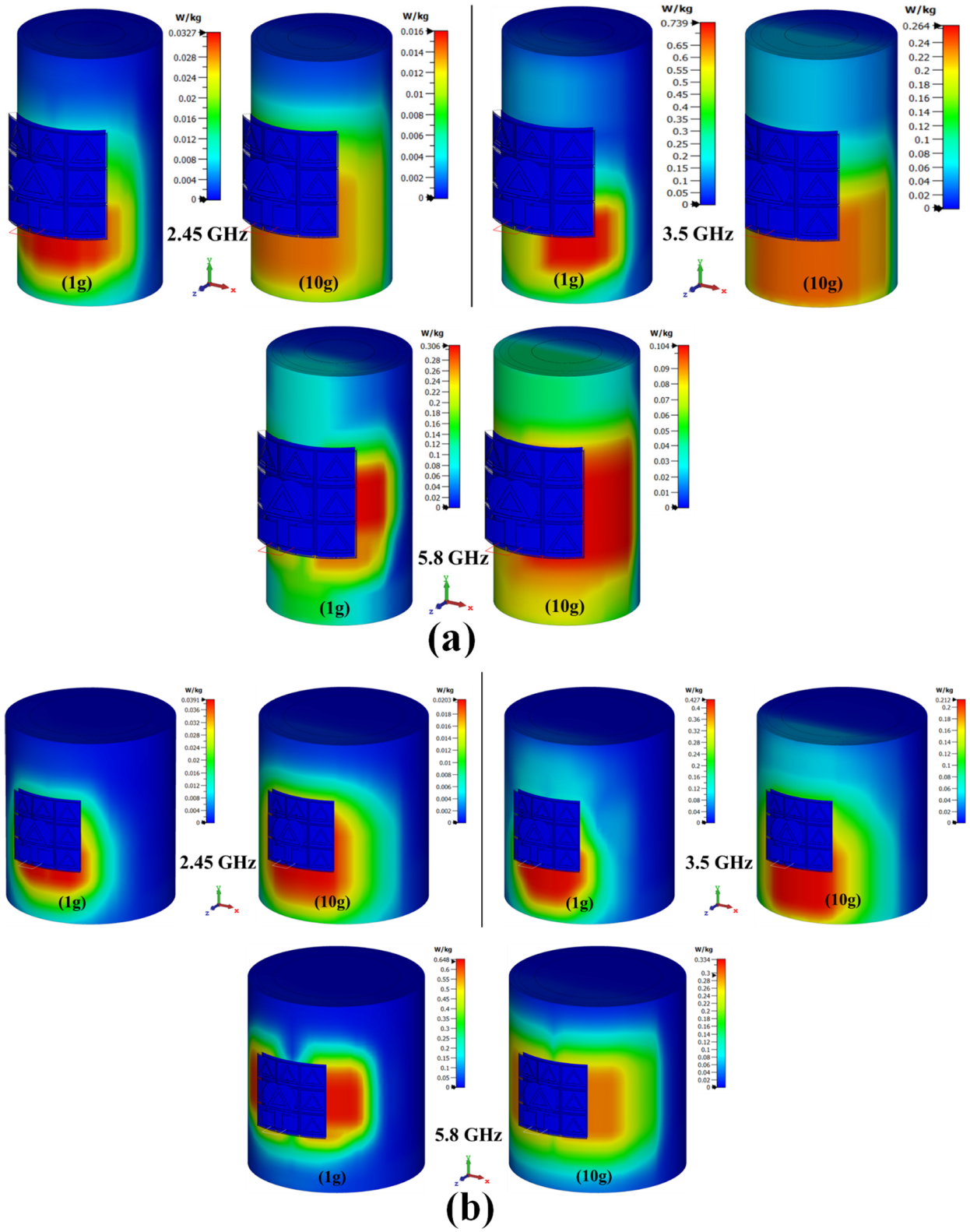


**Figure 21.** *Cont.*

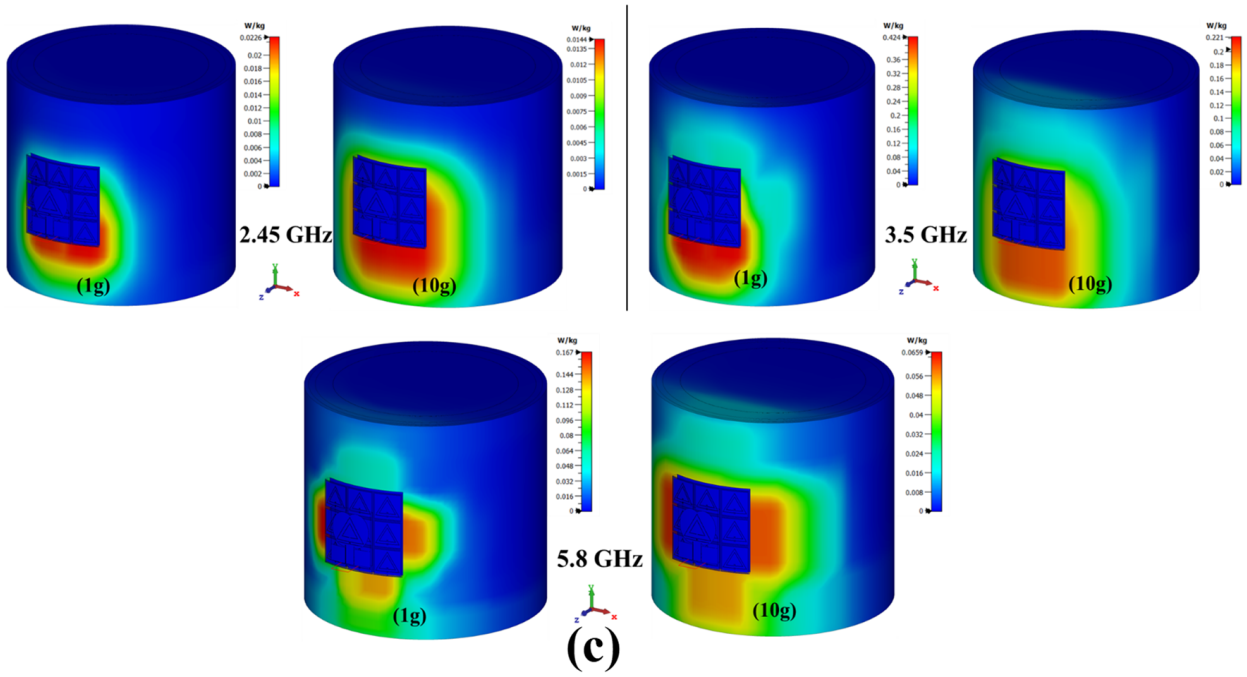


**Figure 21.** SAR values of the UC-EBG-backed antenna curved on (**a**) child arm (worst case: r = 40 mm), (**b**) healthy human arm (r = 60 mm), and (**c**) healthy human leg (r = 70 mm).

**Table 10.** Comparison summary of SAR values for the proposed antenna with and without the UC-EBG plane in different scenarios over 1 g and 10 g of tissue.

| Scenarios | Frequency (GHz) | SAR (W/kg) | |
|---|---|---|---|
| | | 1 g Tissue | 10 g Tissue |
| Antenna without UC-EBG | 2.45 | 15.4 | 10.2 |
| | 3.5 | 16.7 | 12.2 |
| | 5.8 | 17.2 | 13.3 |
| Antenna with UC-EBG (40 mm) | 2.45 | 0.032 | 0.016 |
| | 3.5 | 0.739 | 0.264 |
| | 5.8 | 0.306 | 0.104 |
| Antenna with UC-EBG (60 mm) | 2.45 | 0.039 | 0.02 |
| | 3.5 | 0.427 | 0.021 |
| | 5.8 | 0.648 | 0.334 |
| Antenna with UC-EBG (70 mm) | 2.45 | 0.022 | 0.014 |
| | 3.5 | 0.424 | 0.221 |
| | 5.8 | 0.167 | 0.065 |

Table 11 presents a comparison between the UC-EBG-backed antenna design proposed in this study and other related research papers that have been recently published. The table covers different criteria: antenna size, operating frequencies, substrate material, gain, radiation efficiency, and SAR values over 1 g and 10 g of tissue masses. The comparison demonstrates that the suggested UC-EBG antenna has a compact total size compared to [9–12,34,40–43]. In addition, it surpasses [9,10,34,40–43] in terms of operation frequency bands and [10–12,34,41,43] in terms of higher gain across all resonant frequency bands. Furthermore, it exhibits higher radiation efficiency compared to [9,10,12,40–43], a lower SAR value compared to [9,11,12,34,40–43], and employs a textile material as substrate in contrast to [12,34,41–43].

**Table 11.** Comparison of the present work with previous relevant research works.

| Ref/Year | Total Size ($mm^3$)/($\lambda_g{}^3$) ($\lambda_g$: Guided Waveguide at @2.45 GHz) | Frequency (GHz) | Substrate Material | Textile | Gain (dBi) | Efficiency (%) | Max SAR (W/Kg) | |
|---|---|---|---|---|---|---|---|---|
| | | | | | | | 1 g | 10 g |
| [34]/2023 | 76.5 × 76.5 × 1.6 (1.3 × 1.3 × 0.027) | 2.45/ 5.8 | FR-4 | No | 3.34/ 7.48 | NA | NA | 0.11/ 0.16 |
| [40]/2023 | 122.5 × 122.5 × 1.8 (1.3 × 1.3 × 0.019) | 2.45 | Cotton | Yes | 7.2 | 72 | 0.371 | 0.18 |
| [41]/2023 | 155 ×124 × 0.75 (2.36 × 1.89 × 0.011) | 2.45/ 3.5 | Polyimide | No | 5.4/ 7.5 | 74/ 84 | 0.04/ 0.02 | NA |
| [42]/2022 | 52 × 32 × 1.6 (0.86 × 0.53 × 0.02) | 2.45 | FR-4 | No | 6.87 | 73.68 | NA | 0.68 |
| [9]/2022 | 157 × 157 × 3 (1.54 × 1.54 × 0.029) | 2.45/ 5.4 | Wash cotton | Yes | 7.13/ 7.39 | 62.28/ 64.77 | NA | 1.97/ 1.18 |
| [10]/2022 | 66 × 40 × 4 (0.59 × 0.36 × 0.03) | 2.45/ 5.8 | Felt | Yes | 5.05/ 7.6 | 65/ 75 | 0.034/ 0.014 | 0.018/ 0.032 |
| [11]/2022 | 69 × 69 × 5 (0.61 × 0.61 ×0.04) | 2.45/ 3.5/ 5.8 | Wool felt | Yes | 5.11/ 6.43/ 7.4 | NA | NA | 0.47/ 0.86/ 0.14 |
| [43]/2022 | 61.5 × 61.5 × 1.2 (0.93 × 0.93 × 0.018) | 2.45/ 5.8 | Polyimide | No | 5.37/ 6.89 | 70.5/ 81.5 | 0.35/ 0.39 | NA |
| [12]/2022 | 90 × 90 × 6 (1.34 × 1.34 × 0.09) | 2.45/ 3.5/ 5.8 | Polyimide | No | 4.8/ 5.1/ 6.2 | 70 | 0.34/ 0.07/ 0.33 | NA |
| This paper | 39 × 39 × 2.84 (0.41 × 0.41 × 0.029) | 2.45/ 3.5/ 5.8 | Jeans | Yes | 6.68/ 7.56/ 8.54 | 87.13/ 89.12/ 92.3 | 0.022/ 0.424/ 0.167 | 0.014/ 0.221/ 0.065 |

NA: values were not found.

## 7. Conclusions

A novel triple-band metamaterial-inspired apple-shaped textile antenna backed by the UC-EBG structure is proposed for WBAN and MBAN applications. The proposed antenna is designed for applications requiring operation in the 2.45/3.5/5.8 GHz frequency range. To improve the antenna performance and protect the human body from exposure to antenna back radiation, a plane of 3 × 3 UC-EBG unit cells is proposed. The UC-EBG unit cell has been characterized using a suspended line and dispersion diagram. The antenna and UC-EBG structure are designed based on M-TCSRR and RCSRR metamaterials. They are entirely made from the same textile material (jeans) and have a compact size of 39 × 39 × 2.84 $mm^3$ (0.41 $\lambda_g$ × 0.41 $\lambda_g$ × 0.029 $\lambda_g$), making them easy and comfortable to integrate into clothing. In order to evaluate the antenna performance on human tissues, a phantom model is used to simulate curved body parts, such as arms and legs. The SAR level is reduced when the UC-EBG structure is used behind the antenna as a ground plane, resulting in SAR values below the safety limits set by the FCC and ISED in America and Canada for tissue over 1 g (1.6 W/kg) and recommended by ICNIRP in European Standards for tissue over 10 g (2 W/kg). The proposed wearable antenna design successfully meets the requirements essential for wearable applications. The simulation results showed that the proposed UC-EBG-backed antenna performance is robust and stable in free space and when worn on the body. Its compact size and lightweight design allow it to be easily integrated into wearable electronic devices. The comparison with previous works demonstrated that the proposed UC-EBG-backed antenna offers high gain and efficiency with triple-band coverage, making it an attractive candidate for a variety of MBAN/WBAN applications, including fitness tracking, healthcare monitoring, 5G networks, smart cities, and V2X

communications. Future work is anticipated to enhance this antenna by incorporating techniques to enable circular polarization across the frequency bands.

**Author Contributions:** Conceptualization, T.M. and S.B.; methodology, T.M. and S.B.; software, T.M.; validation, S.B.; formal analysis, T.M., M.S.S., and S.B.; investigation, T.M., S.B., and F.C.; resources, T.M. and S.B.; data curation, T.M. and S.B.; writing—original draft preparation, T.M. and S.B.; writing—review and editing, T.M. and S.B.; supervision, S.B. and F.C.; project administration, M.S.S.; funding acquisition, M.S.S. All authors have read and agreed to the published version of the manuscript.

**Funding:** This research was funded by Taif University, Saudi Arabia, Project No. (TU-DSPP-2024-11).

**Data Availability Statement:** The original contributions presented in the study are included in the article, further inquiries can be directed to the corresponding author.

**Acknowledgments:** The authors extend their appreciation to Taif University, Saudi Arabia, for supporting this work through project number TU-DSPP-2024-11.

**Conflicts of Interest:** The authors declare no conflicts of interest.

## References

1. Berhab, S.; Annou, A.; Chebbara, F. Reconfigurable Low-Profile Antenna-Based Metamaterial for On/Off Body Communications. In *Handbook of Research on Emerging Designs and Applications for Microwave and Millimeter Wave Circuits*; Zbitou, J., Hefnawi, M., Aytouna, F., El Oualkadi, A., Eds.; IGI Global: Hershey, PA, USA, 2023; pp. 166–200. ISBN 978-1-66845-955-3.
2. Hamdi, A.; Nahali, A.; Harrabi, M.; Brahem, R. Optimized Design and Performance Analysis of Wearable Antenna Sensors for Wireless Body Area Network Applications. *J. Inf. Telecommun.* **2023**, *7*, 155–175. [CrossRef]
3. Recent Advancement of Wearable Reconfigurable Antenna Technologies: A Review. Available online: https://ieeexplore.ieee.org/document/9953984/ (accessed on 8 June 2023).
4. Ashyap, A.Y.I.; Elamin, N.I.M.; Dahlan, S.H.; Abidin, Z.Z.; See, C.H.; Majid, H.A.; AL-Fadhali, N.; Mukred, J.A.A.; Saleh, G.; Esmail, B.A.F. Via-Less Electromagnetic Band-Gap-Enabled Antenna Based on Textile Material for Wearable Applications. *PLoS ONE* **2021**, *16*, e0246057. [CrossRef] [PubMed]
5. Ashyap, A.Y.I.; Dahlan, S.H.B.; Zainal Abidin, Z.; Abbasi, M.I.; Kamarudin, M.R.; Majid, H.A.; Dahri, M.H.; Jamaluddin, M.H.; Alomainy, A. An Overview of Electromagnetic Band-Gap Integrated Wearable Antennas. *IEEE Access* **2020**, *8*, 7641–7658. [CrossRef]
6. Wahyuningsih, P.I.; Nur, L.O.; Edwar, E. Wearable Antenna Dual Band with EBG Structure for Health Applications. *CEPAT* **2023**, *7*, 65–72. [CrossRef]
7. Alhuwaidi, S.; Rashid, T. A Novel Compact Wearable Microstrip Patch Antenna for Medical Applications. In Proceedings of the 2020 International Conference on Communications, Signal Processing, and their Applications (ICCSPA), Sharjah, United Arab Emirates, 16–18 March 2021; pp. 1–6.
8. Samal, P.B.; Chen, S.J.; Fumeaux, C. Wearable Textile Multiband Antenna for WBAN Applications. *IEEE Trans. Antennas Propagat.* **2023**, *71*, 1391–1402. [CrossRef]
9. Wajid, A.; Ahmad, A.; Ullah, S.; Choi, D.; Islam, F.U. Performance Analysis of Wearable Dual-Band Patch Antenna Based on EBG and SRR Surfaces. *Sensors* **2022**, *22*, 5208. [CrossRef] [PubMed]
10. Bouamra, W.; Sfar, I.; Mersani, A.; Osman, L.; Ribero, J.-M. Dual-Band Textile AMC Antenna for WLAN/WBAN Applications on the Human Arm. *Int. J. Electron. Telecommun.* **2022**, *68*, 209–216. [CrossRef]
11. El May, W.; Sfar, I.; Ribero, J.M.; Osman, L. Design of Low-Profile and Safe Low SAR Tri-Band Textile EBG-Based Antenna for IoT Applications. *PIER Lett.* **2021**, *98*, 85–94. [CrossRef]
12. Lai, J.; Wang, J.; Sun, W.; Zhao, R.; Zeng, H. A Low Profile Artificial Magnetic Conductor Based Tri-band Antenna for Wearable Applications. *Microw. Opt. Technol. Lett.* **2022**, *64*, 123–129. [CrossRef]
13. Messatfa, T.; Chebbara, F. High-Efficiency 60-GHz Printed Antenna Using a Triple-Layer Metasurface. In *Advanced Computational Techniques for Renewable Energy Systems*; Hatti, M., Ed.; Lecture Notes in Networks and Systems; Springer: Berlin/Heidelberg, Germany, 2023; Volume 591, pp. 160–169. ISBN 978-3-031-21216-1.
14. Falcone, F.; Lopetegi, T.; Baena, J.D.; Marques, R.; Martin, F.; Sorolla, M. Effective Negative-/Spl Epsiv/ Stopband Microstrip Lines Based on Complementary Split Ring Resonators. *IEEE Microw. Wirel. Compon. Lett.* **2004**, *14*, 280–282. [CrossRef]
15. Garg, P.; Jain, P. Metamaterial-Based Patch Antennas—Review. In *Advances in System Optimization and Control*; Singh, S.N., Wen, F., Jain, M., Eds.; Lecture Notes in Electrical Engineering; Springer: Berlin/Heidelberg, Germany, 2019; Volume 509, pp. 65–81. ISBN 9789811306648.
16. Annou, A.; Berhab, S.; Chebbara, F. Metamaterial-Fractal-Defected Ground Structure Concepts Combining for Highly Miniaturized Triple-Band Antenna Design. *J. Microw. Optoelectron. Electromagn. Appl.* **2020**, *19*, 522–541. [CrossRef]

17. Bage, A.; Das, S. Studies of Some Non Conventional Split Ring and Complementary Split Ring Resonators for Waveguide Band Stop & Band Pass Filter Application. In Proceedings of the 2013 International Conference on Microwave and Photonics (ICMAP), Dhanbad, India, 13–15 December 2013; pp. 1–5.
18. Rajkumar, R.; Usha Kiran, K. A Compact Metamaterial Multiband Antenna for WLAN/WiMAX/ITU Band Applications. *AEU-Int. J. Electron. Commun.* **2016**, *70*, 599–604. [CrossRef]
19. Mahendran, K.; Sudarsan, H.; Indhu, R. Design of CSRR-Based Multiband Triangular Patch Antenna for Wireless Applications. In Proceedings of the 2022 13th International Conference on Computing Communication and Networking Technologies (ICCCNT), Kharagpur, India, 3–5 October 2022; pp. 1–5.
20. Smith, D.R.; Vier, D.C.; Koschny, T.; Soukoulis, C.M. Electromagnetic Parameter Retrieval from Inhomogeneous Metamaterials. *Phys. Rev. E* **2005**, *71*, 036617. [CrossRef] [PubMed]
21. Messatfa, T.; Chebbara, F.; Belhedri, A.; Annou, A. A Compact Ultra-Wideband Printed Antenna with CPW Feed for Wireless Applications. *TRE* **2020**, *79*, 1823–1832. [CrossRef]
22. Hasan, M.M.; Rahman, Z.; Shaikh, R.; Alam, I.; Islam, M.A.; Alam, M.S. Design and Analysis of Elliptical Microstrip Patch Antenna at 3.5 GHz for 5G Applications. In Proceedings of the 2020 IEEE Region 10 Symposium (TENSYMP), Dhaka, Bangladesh, 5–7 June 2020; pp. 981–984.
23. Ray, K.P. Design Aspects of Printed Monopole Antennas for Ultra-Wide Band Applications. *Int. J. Antennas Propag.* **2008**, *2008*, 713858. [CrossRef]
24. Rafique, U.; Din, S.u.; Khalil, H. Compact CPW-Fed Super Wideband Planar Elliptical Antenna. *Int. J. Microw. Wirel. Technol.* **2021**, *13*, 407–414. [CrossRef]
25. Garg, R.; Bhartia, P.; Bahl, I.J.; Ittipiboon, A. *Microstrip Antenna Design Handbook*; Artech House: London, UK, 2001; ISBN 0-89006-513-6.
26. Mythili, P.; Das, A. Simple Approach to Determine Resonant Frequencies of Microstrip Antennas. *IEE Proc. Microw. Antennas Propag.* **1998**, *145*, 159–162. [CrossRef]
27. Peddakrishna, S.; Khan, T.; De, A. Electromagnetic Band-Gap Structured Printed Antennas: A Feature-Oriented Survey. *Int. J. RF Microw. Comput. Aided Eng.* **2017**, *27*, e21110. [CrossRef]
28. Goussetis, G.; Feresidis, A.P.; Vardaxoglou, J.C. FSS Printed on Grounded Dielectric Substrates: Resonance Phenomena, AMC and EBG Characteristics. In Proceedings of the 2005 IEEE Antennas and Propagation Society International Symposium, Washington, DC, USA, 3–8 July 2005; Volume 1, pp. 644–647.
29. Rogers, S.; McKinzie, W.; Mendolia, G. AMCs Comprised of Interdigital Capacitor FSS Layers Enable Lower Cost Applications. In Proceedings of the IEEE Antennas and Propagation Society International Symposium, Columbus, OH, USA, 22–27 June 2003; Volume 2, pp. 411–414.
30. Wang, E.; Liu, Q. GPS Patch Antenna Loaded with Fractal EBG Structure Using Organic Magnetic Substrate. *PIER Lett.* **2016**, *58*, 23–28. [CrossRef]
31. Yang, F.; Rahmat-Samii, Y. *Electromagnetic Band Gap Structures in Antenna Engineering*; Cambridge University Press: Cambridge, UK, 2008; ISBN 978-0-521-88991-9.
32. Rezaei, A.M.; Rezaei, P. EBG Structures Properties and Their Application to Improve Radiation of a Low Profile Antenna. *JIST* **2013**, *1*, 251–259. [CrossRef]
33. Youssef, O.M.; Atrash, M.E.; Abdalla, M.A. A Compact Fully Fabric I-Shaped Antenna Supported with Textile-Based AMC for Low SAR 2.45 GHz Wearable Applications. *Microw. Opt. Technol. Lett.* **2023**, *65*, 2021–2030. [CrossRef]
34. Du, C.; Pei, L.-R.; Zhang, J.; Shi, C.-X. A Gain Enhanced Dual-Band Low SAR AMC-Based MIMO Antenna for WBAN and WLAN Applications. *Prog. Electromagn. Res. M* **2023**, *115*, 21–34. [CrossRef]
35. Ashyap, A.Y.I.; Zainal Abidin, Z.; Dahlan, S.H.; Majid, H.A.; Saleh, G. Metamaterial Inspired Fabric Antenna for Wearable Applications. *Int. J. RF Microw. Comput. Aided Eng.* **2019**, *29*, e21640. [CrossRef]
36. Gao, G.-P.; Hu, B.; Wang, S.-F.; Yang, C. Wearable Circular Ring Slot Antenna with EBG Structure for Wireless Body Area Network. *IEEE Antennas Wirel. Propag. Lett.* **2018**, *17*, 434–437. [CrossRef]
37. Gabriel, C.; Gabriel, S. *Compilation of the Dielectric Properties of Body Tissues at RF and Microwave Frequencies*; King's College, London, Department of Physics: London, UK, 1996; p. 273.
38. Ahmad, A.; Faisal, F.; Ullah, S.; Choi, D.-Y. Design and SAR Analysis of a Dual Band Wearable Antenna for WLAN Applications. *Appl. Sci.* **2022**, *12*, 9218. [CrossRef]
39. Ahmad, S.; Paracha, K.N.; Sheikh, Y.A.; Ghaffar, A.; Butt, A.D.; Alibakhshikenari, M.; Soh, P.J.; Khan, S.; Falcone, F. A Metasurface-Based Single-Layered Compact AMC-Backed Dual-Band Antenna for Off-Body IoT Devices. *IEEE Access* **2021**, *9*, 159598–159615. [CrossRef]
40. Ayd, R.; Saad, A.; Hassan, W.M.; Ibrahim, A.A. A Monopole Antenna with Cotton Fabric Material for Wearable Applications. *Sci. Rep.* **2023**, *13*, 7315. [CrossRef]
41. Yang, S.; Yu, C.; Yang, X.; Zhao, J. A Tri-Band Flexible Antenna Based on Tri-Band AMC Reflector for Gain Enhancement and SAR Reduction. *AEU-Int. J. Electron. Commun.* **2023**, *168*, 154715. [CrossRef]

42. Le, M.T.; Tran, T.P.; Nguyen, Q.C. Wearable BLE Wireless Sensor Based on U-Shaped EBG Monopole Antenna. *J. Sens.* **2022**, *2022*, 8593750. [CrossRef]
43. Wang, S.; Gao, H. A Dual-Band Wearable Conformal Antenna Based on Artificial Magnetic Conductor. *Int. J. Antennas Propag.* **2022**, *2022*, 9970477. [CrossRef]